Computer Methods in Applied Mechanics and Engineering 426 (2024) 116972

Contents lists available at ScienceDirect

Comput. Methods Appl. Mech. Engrg.

journal homepage: www.elsevier.com/locate/cma

Phase field modeling of hyperelastic material interfaces – Theory, implementation and application to phase transformations

Hendrik Wilbuer, Patrick Kurzeja, Jörn Mosler *

Institute of Mechanics, TU Dortmund University, Leonhard-Euler-Str. 5, Dortmund, D-44227, Germany

ARTICLE INFO

Keywords:
Surface elasticity theory
Interface elasticity
Phase field theory
Phase transformation
Incremental energy minimization
Finite element method

ABSTRACT

Interface mechanics can significantly govern the evolution of multiple phases on smaller scales, e.g., determining the properties of TWIP- and TRIP-steels, geopolymers or Li-ion batteries. The present contribution is specifically centered around the influence of interface elasticity on mechanically induced phase transformations. A geometrically exact finite element framework is developed for this purpose based on incremental energy minimization. It is set up in three-dimensional space and comprises an Allen-Cahn type phase field formulation based on a Modica-Mortola double-well functional, as well as a Ginzburg-Landau type viscosity formulation. The phase field approximation of the interface deformation gradient is derived by means of homogenization theory. A monolithic solver is employed for the resulting set of non-linear coupled equations. The example of coalescing spheres shows that larger interface energies can amplify and accelerate coalescence. Lower interface energies, in contrast, allow for distinct spreading of the energetically favorable bulk phase. Deformation-dependent interface energies particularly add stress peaks to this process that are localized at the phase transition zone. The relaxation of a stepped interface shape showed that deformation-dependent interface energies favor a plane partition of the bulk phases. Yet, they also delay breakup events compared to simple constant interface energies. This peculiarity can be beneficial for calibration purposes. Strain dependence moreover causes an additional elastic stiffness in the direction of the interface tangent plane and constitutes thus another origin for anisotropy of the overall structure.

1. Introduction

This treatise analyzes the role of interface elasticity in mechanically induced phase transformations due to the increasing relevance of interface mechanics for materials on smaller length scales. The effective properties of some materials explicitly rely on the evolution of their phase structure, for example, the so-called TWIP- or TRIP-steels [1], growth stress in trees [2] or geopolymers [3]. Whenever the mechanical evolution on the micro scale is supposed to be studied, though, the interaction of different phases on the micro level needs to be taken into account explicitly. More importantly, interface mechanics play a key role due to the large interface-to-volume ratio. This applies, for instance, to formation of metallic surfaces [4,5], disconnection-mediated interface migration interfaces [6,7], anchoring of nematic liquid crystals [8], minimal surface energy structures [9] or lithiation of amorphous silicon nanospheres for the design of batteries [10]. Despite the abundant applications, the effect of deformable elastic interfaces nevertheless still needs to be explored further. A framework was originally introduced in a continuum mechanics context in [11] and has been well established ever since, see e.g. [12,13]. Further developments are found for the description of cohesive and coherent interfaces [14]. While cohesive interfaces can be used in damage/fracture mechanics [15,16], coherent interfaces are

* Corresponding author.
E-mail address: joern.mosler@tu-dortmund.de (J. Mosler).

https://doi.org/10.1016/j.cma.2024.116972
Received 21 December 2023; Received in revised form 22 February 2024; Accepted 28 March 2024
Available online 23 April 2024
0045-7825/© 2024 The Author(s). Published by Elsevier B.V. This is an open access article under the CC BY license (http://creativecommons.org/licenses/by/4.0/).

usually found in models in regard to phase transformation, see e.g. [17,18]. The work at hand now focuses on a systematic study of the impact of deformable elastic coherent interfaces on the evolution of bi-phasic structures.

One possible approach to predict interface-dominated microstructural evolution, is to employ and implement a phase field scheme. In general, there are two classical types of phase field approaches, namely the Cahn-Hilliard type and Allen-Cahn type (based on their work in [19,20]). While the first one is mass conserving, the latter one is not. Although the framework presented in this paper can be applied to both types, focus is here on displacive phase transformations. Accordingly, an Allen-Cahn-type model is chosen. Compared to sharp-interface descriptions like XFEM [21] or sharp interface *finite element* (FE) models, the choice of a diffuse phase field formulation also comes along with individual advantages. Most importantly, it still allows for the consideration of phase transformations and tracking of the interface motion. When this is combined with a suitable homogenization scheme for the bulk superposition, the model can also automatically enforce static as well kinematic compatibility in the interface.

The present work hence develops a phase field framework that allows to explore the effects of deformation-dependent interface elasticity. Its key results are:

- a variational phase field framework for deformation-dependent interface elasticity, including phase transformations,
- phase field approximation of the interface deformation gradient by means of homogenization theory,
- a corresponding finite element implementation within a finite strain setting,
- interface energy can be counteracting bulk-induced phase transformation in coalescence processes,
- delayed breakup due to deformation-dependent interfaces which can serve as an indicator for experimental calibration.

The subsequent Section 2 will first introduce the fundamentals of sharp interfaces, before Section 3 derives the diffuse phase field approximation. Section 4 will present the finite element implementation. Sections 5 and 6 provide numerical examples for the coalescence of inclusions and the breakup of a stepped interface, respectively. Their discussion emphasizes the time evolution of shape and energy contributions before Section 7 concludes the main findings.

2. Fundamentals of sharp interfaces

The following section introduces the notation, kinematics and balance equations of two distinct bulk phases separated by a sharp interface. Such descriptions can be useful, for instance, for two crystals of different orientation [22] or the more application-oriented consideration of the microstructure of TWIP-/TRIP-steels [23]. Peculiarities of these motivating examples will be neglected for the sake of focused illustration of interface effects, though, e.g. neglecting transformation strains. The following formulation will serve as a more general starting point for the later phase field description.

2.1. Kinematics

$\mathcal{B}$ is a domain in space with $\mathcal{B}_0$ representing the domain in reference configuration and $\mathcal{B}_t$ referring to the spatial configuration at time t, see Fig. 1. The bulk phases follow standard notation, i.e. each point $\boldsymbol{X}$ in the reference configuration is mapped to the spatial configuration using the nonlinear deformation mapping

$$\boldsymbol{x} = \boldsymbol{\varphi}(\boldsymbol{X}). \tag{1}$$

The corresponding deformation gradient

$$\boldsymbol{F} = \mathrm{Grad}\,(\boldsymbol{\varphi}(\boldsymbol{X})) = \frac{\partial\,\boldsymbol{\varphi}(\boldsymbol{X})}{\partial\,\boldsymbol{X}} = \frac{\partial\,\boldsymbol{x}}{\partial\,\boldsymbol{X}} \tag{2}$$

projects line increments via $\mathrm{d}\boldsymbol{x} = \boldsymbol{F}\cdot\mathrm{d}\boldsymbol{X}$. Area and volume elements are mapped via the cofactor $\mathrm{Cof}(\boldsymbol{F}) = \mathrm{Det}(\boldsymbol{F})\,\boldsymbol{F}^{-\mathrm{T}}$ and the determinant $\mathrm{Det}(\boldsymbol{F})$ of the deformation gradient, i.e., $\mathrm{d}\boldsymbol{a} = \mathrm{Cof}(\boldsymbol{F})\cdot\mathrm{d}\boldsymbol{A}$ and $\mathrm{d}v = \mathrm{Det}(\boldsymbol{F})\,\mathrm{d}V$.

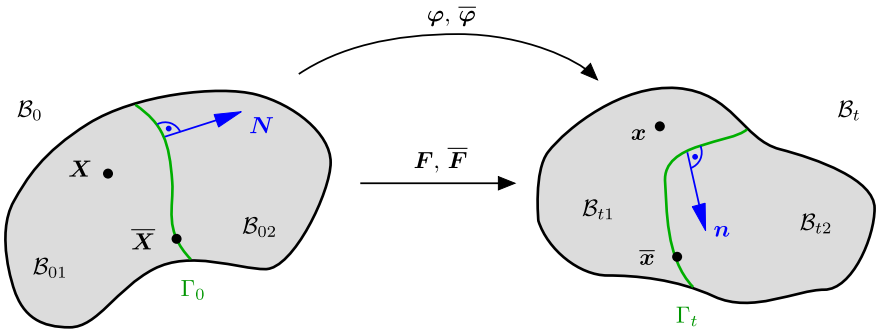

Fig. 1. Visualization of the reference configuration (at time t_0) and spatial configuration (at time t) of an exemplary body $\mathcal{B}$, which consists of two bulk phases and one interface Γ.

The analogous interface quantities will be denoted by $\overline{\{\bullet\}}$. They follow the seminal work in [11,24], while corresponding notation and the necessary derivations here are largely based on [14,25]. Assuming that the interface follows the bulk deformations, the interface deformation gradient $\overline{\boldsymbol{F}}$ is determined from the bulk deformation gradient $\boldsymbol{F}$ by

$$\overline{\boldsymbol{F}} = \boldsymbol{F} \cdot \overline{\boldsymbol{I}} = \boldsymbol{F} \cdot [\boldsymbol{I} - \boldsymbol{N} \otimes \boldsymbol{N}]. \tag{3}$$

$\boldsymbol{I}$ is the identity tensor and $\overline{\boldsymbol{I}}$ is the interface identity tensor. The latter is of rank 2 and maps onto the interface tangent vectors, omitting out-of-plane components in the normal direction. The mapping of line elements between the interface configurations then reads

$$\overline{\boldsymbol{x}} = \overline{\boldsymbol{\varphi}}(\overline{\boldsymbol{X}}) \tag{4}$$

and

$$\overline{\boldsymbol{F}} = \overline{\mathrm{Grad}}\left(\overline{\boldsymbol{\varphi}}(\overline{\boldsymbol{X}})\right) = \frac{\partial \overline{\boldsymbol{\varphi}}(\overline{\boldsymbol{X}})}{\partial \overline{\boldsymbol{X}}} = \frac{\partial \overline{\boldsymbol{x}}}{\partial \overline{\boldsymbol{X}}}. \tag{5}$$

The interface determinant can be finally defined by the covariant basis vector set within the interface, $\left\{\overline{\boldsymbol{G}}_1, \overline{\boldsymbol{G}}_2\right\}$, reading

$$\overline{\mathrm{Det}}\left(\overline{\{\bullet\}}\right) = \frac{|\overline{\{\bullet\}} \cdot \overline{\boldsymbol{G}}_1 \times \overline{\{\bullet\}} \cdot \overline{\boldsymbol{G}}_2|}{|\overline{\boldsymbol{G}}_1 \times \overline{\boldsymbol{G}}_2|}. \tag{6}$$

The invariant $\overline{\mathrm{Det}}\left(\overline{\boldsymbol{F}}\right)$ is particularly relevant for interface descriptions, because it maps area elements between the two configurations and therefore depicts the area ratio between the interface elements of spatial and reference configuration [26].

2.2. Balance equations and 2nd law of thermodynamics

The bulk phases and the interface need to fulfill the standard balance equations. An overview of detailed derivations can be found in [27], on which the following paragraphs are based on.

Under the quasi-static assumption of negligible inertia terms, the balance of linear momentum inside the bulk phases reads

$$\mathrm{Div}(\boldsymbol{P}) + \boldsymbol{B} = \boldsymbol{0} \quad \Leftrightarrow \quad \mathrm{div}(\boldsymbol{\sigma}) + \boldsymbol{b} = \boldsymbol{0}. \tag{7}$$

It is provided in two formats, where $\boldsymbol{P}$ represents the first Piola-Kirchhoff stress tensor and $\boldsymbol{\sigma}$ represents the spatial Cauchy stress tensor. $\boldsymbol{B}$, $\boldsymbol{b}$ represent body forces in referential or spatial configuration, respectively, and the same applies to the divergence operators Div(•), div(•). The balance of angular momentum can be directly reformulated into a symmetry condition of the stress tensor of the form

$$\boldsymbol{F} \cdot \boldsymbol{P}^{\mathrm{T}} = \boldsymbol{P} \cdot \boldsymbol{F}^{\mathrm{T}} \quad \Leftrightarrow \quad \boldsymbol{\sigma} = \boldsymbol{\sigma}^{\mathrm{T}}. \tag{8}$$

The analogous interface balance equations of linear momentum and angular momentum read, respectively,

$$\overline{\mathrm{Div}}(\overline{\boldsymbol{P}}) + \overline{\boldsymbol{B}} + [\![\boldsymbol{P}]\!] \cdot \boldsymbol{N} = \boldsymbol{0} \quad \Leftrightarrow \quad \overline{\mathrm{div}}(\overline{\boldsymbol{\sigma}}) + \bar{\boldsymbol{b}} + [\![\boldsymbol{\sigma}]\!] \cdot \boldsymbol{n} = \boldsymbol{0} \tag{9}$$

and

$$\overline{\boldsymbol{F}} \cdot \overline{\boldsymbol{P}}^{\mathrm{T}} = \overline{\boldsymbol{P}} \cdot \overline{\boldsymbol{F}}^{\mathrm{T}} \quad \Leftrightarrow \quad \overline{\boldsymbol{\sigma}} = \overline{\boldsymbol{\sigma}}^{\mathrm{T}}. \tag{10}$$

$[\![\boldsymbol{P}]\!] = \boldsymbol{P}_2 - \boldsymbol{P}_1$ (or $[\![\boldsymbol{\sigma}]\!] = \boldsymbol{\sigma}_2 - \boldsymbol{\sigma}_1$, respectively) denotes the jump in the stresses between the two bulk phases and the remaining quantities represent the analogous interface quantities.

The balance equations for linear momentum will be enforced later in the finite element implementation. Balance of angular momentum on the other hand is fulfilled a priori, if the free Helmholtz energy potential is a function depending only on the right Cauchy-Green strain tensors $\boldsymbol{C}$ or $\overline{\boldsymbol{C}}$, respectively, i.e. the principle of material frame indifference holds.

The volume-specific free Helmholtz energies of bulks and interfaces are denoted by ψ and $\overline{\psi}$, respectively. They define their total (integrated) counterparts Ψ and $\overline{\Psi}$, as well as the total free Helmholtz energy of the mechanical system as

$$\Psi_{\mathrm{tot,sharp}} := \Psi + \overline{\Psi} \tag{11}$$

$$= \int_{\mathcal{B}_{01}} \psi_1 \, \mathrm{d}V + \int_{\mathcal{B}_{02}} \psi_2 \, \mathrm{d}V + \int_{\Gamma_0} \overline{\psi} \, \mathrm{d}A. \tag{12}$$

Special emphasis will be put later on the elastic energy $\overline{\psi}(\overline{\boldsymbol{C}})$ of the deformable interfaces.

The second law of thermodynamics is used for a thermodynamically consistent derivation of constitutive relations [28]. Omitting detailed derivations and assuming an isothermal setting, the Clausius-Duhem inequalities read

$$\mathcal{D} = \boldsymbol{P} : \mathrm{Grad}(\dot{\boldsymbol{\varphi}}) - \dot{\psi} \geq 0 \quad \text{and} \quad \bar{\mathcal{D}} = \overline{\boldsymbol{P}} : \overline{\mathrm{Grad}}(\dot{\overline{\boldsymbol{\varphi}}}) - \dot{\overline{\psi}} \geq 0, \tag{13}$$

where $\dot{\{\bullet\}}$ indicates the material time derivative.

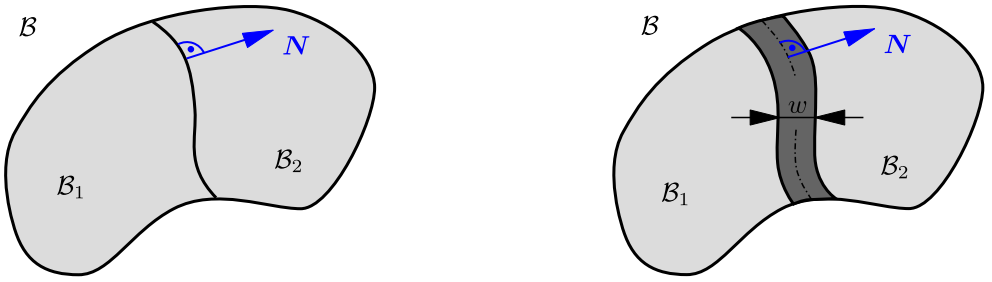

(a) sharp interface, no intersection of the phases **(b)** diffuse interface with transition zone between $\mathcal{B}_1$ and $\mathcal{B}_2$

Fig. 2. Visualization of two distinct phases inside a domain $\mathcal{B}$ separated by (a) a sharp interface (zero width) and (b) a diffuse interface (finite width w), respectively.

3. Phase field approximation of interface elasticity

Complementing sharp-interface descriptions [11,21], diffuse interfaces can be used for at least two reasons. From the mechanical perspective, real interfaces can show a finite and diffuse spatial distribution on smaller scales, e.g., phase transition zones or sintering contacts [29,30]. From the methodological perspective, control of the interface width can be beneficial, e.g., for regularization of otherwise ill-posed damage models [31–33]. The present work will use a diffuse approximation of the interface, namely, by the well-established phase field method. To be more specific, a non-conserving Allen-Cahn type phase field model [19] will be considered in what follows. However, this choice is not mandatory. The presented incorporation of deformation-dependent material interfaces can also be applied directly to Cahn-Hilliard-type models.

Before we proceed with the phase field formulation, we find it helpful to summarize the main assumptions of this investigation. They are applied to lay the focus on the deformation-dependent interface elasticity and to not obscure the related effects. The basis is a fully elastic framework that can be compared and combined with well-established phase field frameworks in literature. Firstly, transformation strains of the displacive phase transformations are neglected but can be accounted for, e.g., in the form of Bain strains. Secondly, the order parameter represents the relative mass fraction, i.e. the pre-factors in Eq. (16) depend linearly on p. Thirdly, the Taylor-Voigt assumption is used for the description of the displacement jump and yields the same interface deformation gradient like a homogenization based on rank-1 or partial rank-1. These individual assumptions are discussed in the following in more detail where they apply.

3.1. Phase field parametrization

A set of order parameters (also called phase field variables) $p_i \in [0,\ 1]$ is introduced for the distinction of the phases $i \in \{1,\ 2\}$. They can be interpreted as a volume fraction of phase i in the present analysis, but other weightings such as densities are also possible. Considering that the present setup only consists of two different phases and exploiting the partition of unity, the parametrization can be simplified to a single order parameter p by setting

$$p_1 := 1 - p \quad \text{and} \quad p_2 := p \quad \text{with} \quad p_1 + p_2 = 1. \tag{14}$$

In contrast to sharp interfaces (see Fig. 2(a)), two bulk phases coexist within the diffuse interface region. The relative volume fractions of the two phases are measured by phase field p. They are gradually inverted in the direction of the normal vector, now defined as

$$\boldsymbol{N}(\nabla p) = \frac{\nabla p}{\|\nabla p\|}. \tag{15}$$

The sub-domains overlap ($\mathcal{B}_1 \cap \mathcal{B}_2 \neq \varnothing$) in the smooth transition zone, where $p \in]0,\ 1[$. This yields a non-zero interface width w, cf. Fig. 2(b).

3.2. Homogenization of the bulk phases

As a first result of the diffuse-interface approach, the superposition of bulk phases in the transition zone requires a mixing rule, or more physically, a homogenized description. In general, the homogenization can account for various mixtures of individual energies $\psi_i(\boldsymbol{F},\ p)$, which can be implemented into the presented framework. Putting the focus on interface mechanics, though, we follow the implications in [34] and use a linear superposition of Helmholtz free energies between phase 1 ($p = 0$) and phase 2 ($p = 1$) of the form

$$\psi = p_1\,\psi_1 + p_2\,\psi_2 = [1 - p]\,\psi_1 + p\,\psi_2. \tag{16}$$

Analogously, the superposed bulk deformation gradient is set to

$$\boldsymbol{F} = [1-p]\,\boldsymbol{F}_1 + p\,\boldsymbol{F}_2. \tag{17}$$

Higher order interpolation functions can yield vanishing driving forces in fully developed phases, $p = 0$ and $p = 1$, see [35,36]. The present analysis yet employs a linear interpolation.

Eq. (17) can be reformulated by the jump of the deformation gradient $[\![\boldsymbol{F}]\!]$ to read

$$[\![\boldsymbol{F}]\!] = \boldsymbol{F}_2 - \boldsymbol{F}_1 \quad \Rightarrow \quad \boldsymbol{F}_1 = \boldsymbol{F} - p\,[\![\boldsymbol{F}]\!], \quad \boldsymbol{F}_2 = \boldsymbol{F} + [1-p]\,[\![\boldsymbol{F}]\!]. \tag{18}$$

There are several homogenization approaches for the determination of $[\![\boldsymbol{F}]\!]$ itself throughout the literature, which relate to respective classes of physical compatibility. Four distinct ones (for a more detailed discussion refer to [37]) are

$$[\![\boldsymbol{F}]\!] = \begin{cases} \boldsymbol{0}, & \text{Taylor-Voigt} \\ \boldsymbol{a}\otimes\boldsymbol{N}, \quad \text{with} \quad \boldsymbol{a},\,\boldsymbol{N} = \arg\{\min_{\boldsymbol{a},\,\boldsymbol{N}}(\psi)\}, & \text{rank-1} \\ \boldsymbol{a}\otimes\boldsymbol{N}, \quad \text{with} \quad \boldsymbol{a} = \arg\{\min_{\boldsymbol{a}}(\psi)\} \quad \text{and} \quad \boldsymbol{N} = \dfrac{\nabla p}{\|\nabla p\|}, & \text{partial rank-1} \\ \arg\{\min_{[\![\boldsymbol{F}]\!]}(\psi)\}, & \text{Reuss-Sachs,} \end{cases} \tag{19}$$

where $\boldsymbol{a}$ is a so-called jump vector.

When kinematic compatibility is enforced by $[\![\boldsymbol{F}]\!] = \boldsymbol{a}\otimes\boldsymbol{N}$ (which holds for both rank-1 assumptions), the jump in the deformation gradient mapped into the tangential space (using $\overline{\boldsymbol{I}}$, cf. Eq. (3)) simplifies to

$$\begin{aligned} &\boldsymbol{F}_2 - \boldsymbol{F}_1 && = [\![\boldsymbol{F}]\!] = \boldsymbol{a}\otimes\boldsymbol{N} \\ \Rightarrow\ &\overline{\boldsymbol{F}}_2 - \overline{\boldsymbol{F}}_1 && = [\![\boldsymbol{F}]\!]\cdot\overline{\boldsymbol{I}} = \boldsymbol{a}\otimes\boldsymbol{N}\cdot[\boldsymbol{I}-\boldsymbol{N}\otimes\boldsymbol{N}] = \boldsymbol{a}\otimes\boldsymbol{N} - \boldsymbol{a}\otimes\boldsymbol{N} = \boldsymbol{0} \\ \Rightarrow\ &\overline{\boldsymbol{F}}_1 = \overline{\boldsymbol{F}}_2 = \overline{\boldsymbol{F}}, \end{aligned} \tag{20}$$

using identity $\boldsymbol{N}\cdot\boldsymbol{N} = 1$. The same result can be achieved analogously for the Taylor-Voigt assumption (special case of kinematic compatibility $\boldsymbol{a} = \boldsymbol{0}$, although the calculation is trivial due to the resulting $[\![\boldsymbol{F}]\!] = \boldsymbol{0}$). Only in the case of Reuss-Sachs this does not hold. Accordingly, the Taylor-Voigt assumption as well as both rank-1 assumptions result in the same interface deformation gradients within both phases, $\overline{\boldsymbol{F}}_1 = \overline{\boldsymbol{F}}_2$. These gradients are identical to their macroscopic counterpart $\overline{\boldsymbol{F}}$.

Because this work focuses on in-plane interface energies and not on the bulk homogenization itself, the Taylor-Voigt assumption is chosen for the sake of simplicity. Eq. (16) is thus specified to read

$$\Psi = \Psi(\boldsymbol{F}, p) = \int_{\mathcal{B}_0} \psi(\boldsymbol{F}, p)\,\mathrm{d}V = \int_{\mathcal{B}_0} [1-p]\,\psi_1(\boldsymbol{F}) + p\,\psi_2(\boldsymbol{F})\,\mathrm{d}V \tag{21}$$

in the integral form. The remaining options are certainly also feasible.

Remark 1. The considered phase transformations processes are of displacive type, which can be typically associated with transformation strains. An implementation is possible, e.g., in terms of Bain strains as shown in [35]. The present analysis however neglects this effect to keep the focus on the diffuse hyperelastic interface. A heterogeneity of the separated bulk phases is instead accounted for by variations of the ratio of the elastic moduli, which allows a more systematic analysis of the individual influences.

3.3. Diffuse interface energy

With the phase field parametrization and bulk description at hand, the focus will now be placed on the diffuse interface itself. The starting point is a so-called double-well potential as proposed in [38] – in designation to the authors also referred to by the name *Modica-Mortola functional* –

$$f_{\mathrm{dw}} = \frac{6}{w}\,p^2\,[1-p]^2 + \frac{3}{2}\,w\,\|\nabla p\|^2. \tag{22}$$

The basic principle has ever since been adapted to diffuse phase fields [19]. It approximates a sharp interface by the phase field parameter p, its referential gradient in space $\nabla p = \partial p/\partial\boldsymbol{X}$ and the interface width w. More importantly, it was proven that the volume integral of this functional Γ-converges to the sharp-interface limit for $w \to 0$ [38–40]. For the interested reader, a convergence study is provided in Appendix A.2. It can also be shown, that the minimization of the double-well functional w.r.t. p (under suitable boundary conditions) yields a sigmoid-type transition function, $p(d) = \left[\tanh(d/w) + 1\right]/2$, see [37].

The key variation of the present analysis is the (local) interface energy $\overline{\psi}$. For the implementation into the phase field setting, it is combined with the diffuse interface approximation via the double-well potential as

$$\overline{\psi}_{\mathrm{dw}} := f_{\mathrm{dw}}\,\overline{\psi}. \tag{23}$$

Note the dependence of this combined interface energy on strains as well as on the phase field parameter and its gradient via $\overline{\psi}_{\mathrm{dw}}(\overline{\boldsymbol{F}}(\boldsymbol{F}, \boldsymbol{N}(\nabla p)), p, \nabla p)$. The total (integrated) interface energy

$$\overline{\Psi} = \int_{\mathcal{B}} \overline{\psi}_{\mathrm{dw}}\,\mathrm{d}V, \tag{24}$$

then accordingly approximates the sharp-interface integral (cf. Eqs. (11) and (12)) by a volume integral.

3.4. Rate potential and incremental formulation

A variationally consistent framework for the model will be derived in the subsequent steps. The energy terms have so far almost exclusively been discussed as specific quantities in terms of continua or rather on a local material point level. Shifting the focus from the material point to the global level, the different contributions are summed up and integrated over the domain $\mathcal{B}$. This yields the total global (integrated) free Helmholtz energy

$$\Psi_{\text{tot}} = \Psi + \overline{\Psi} \tag{25}$$

as well as the global/total rate potential

$$\begin{aligned} \dot{\mathcal{I}} :&= \dot{\mathcal{I}}_{\text{red}} && - \mathcal{P}_{\text{ext}} \\ &= \dot{\Psi} + \dot{\overline{\Psi}} + \dot{H} + \int_{\mathcal{B}_0} \phi \, \mathrm{d}V && - \mathcal{P}_{\text{ext}}, \end{aligned} \tag{26}$$

where the first two terms are the rates of the bulk and interface energies of the domain $\mathcal{B}$, see Eqs. (21) and (24). $\mathcal{P}_{\text{ext}}$ represents the rate of external work

$$\mathcal{P}_{\text{ext}} = \dot{\mathcal{W}}_{\text{ext}} \qquad \text{with} \qquad \mathcal{W}_{\text{ext}} = \int_{\mathcal{B}_0} \rho_0 \, \boldsymbol{B} \cdot \boldsymbol{\varphi} \, \mathrm{d}V + \int_{\partial \mathcal{B}_0} \boldsymbol{T} \cdot \boldsymbol{\varphi} \, \mathrm{d}A. \tag{27}$$

due to body forces $\boldsymbol{B}$ and external tractions/loads $\boldsymbol{T}$.

In addition to that, a penalty term

$$H = \int_{\mathcal{B}_0} h(p) \, \mathrm{d}V \tag{28}$$

has been implemented, because the double-well functional from Eq. (22) does not suffice to limit the order parameter to the interval $p \in [0,\ 1]$ by respective penalization of p and ∇p. H originates from a local penalty function

$$h(p) = \begin{cases} \frac{1}{2} \, h_{\text{pen}} \, [p - [1 - h_{\text{off}}]]^2, & \text{if } p \geq 1 - h_{\text{off}} \\ \frac{1}{2} \, h_{\text{pen}} \, [p - h_{\text{off}}]^2, & \text{if } p \leq h_{\text{off}} \\ 0, & \text{otherwise,} \end{cases} \tag{29}$$

where h_{pen} represents the constant penalty parameter. Here, a standard penalty approach was extended by a constant offset of $h_{\text{off}} = 5 \cdot 10^{-3}$ in order to prevent unphysical values of p in practice. Alternatively, constraint $p \in [0,\ 1]$ can also be strictly enforced – as shown by one of the authors, [35].

Because phase transformations are typically associated with additional dissipation, the latter needs to be considered for the model as well. A dissipation functional is thus intended to restrict the rate of the phase transformation and thus effectively limits the speed at which the interface can move through the bulk domain $\mathcal{B}$. Therefore, a not yet specified dissipation functional $\phi(\dot{p})$ has been added to the system's rate potential (cf. Eq. (26)), which renders the system rate dependent. Please note that the present analysis focuses on quasi-static transformations. Inertia terms are thus neglected and the only relevant time scales are due to dissipation (later specified via viscosity η) and the loading rate. The time evolution of the resulting phase transformations will be discussed in detail in the final examples.

The integration of Eq. (26) over time interval $\Delta t = [t_n,\ t_{n+1}]$ yields

$$\begin{aligned} \Delta \mathcal{I} := \int_{t_n}^{t_{n+1}} \dot{\mathcal{I}} \, \mathrm{d}t &= \Psi(t_{n+1}) - \Psi(t_n) + \overline{\Psi}(t_{n+1}) - \overline{\Psi}(t_n) + H(t_{n+1}) - H(t_n) \\ &\quad - \mathcal{W}_{\text{ext}}(t_{n+1}) + \mathcal{W}_{\text{ext}}(t_n) + \int_{\mathcal{B}_0} \int_{t_n}^{t_{n+1}} \phi(\dot{p}) \, \mathrm{d}t \, \mathrm{d}V. \end{aligned} \tag{30}$$

Since the later FE problem needs to be solved in an incremental manner, the incremental formulation will be used for the implementation into the FE framework. Because the original bulk and interface mechanics are based on hyperelastic potentials, the only rate occurring here is that of the phase field parameter for the dissipation contribution. It will be approximated by $\dot{p} \approx (p(t_{n+1}) - p(t_n))/\Delta t$ and the corresponding integral dissipation term then results in

$$\int_{\mathcal{B}_0} \int_{t_n}^{t_{n+1}} \phi(\dot{p}) \, \mathrm{d}t \, \mathrm{d}V \approx \int_{\mathcal{B}_0} \Delta t \, \phi \left(\frac{p(t_{n+1}) - p(t_n)}{\Delta t} \right) \mathrm{d}V. \tag{31}$$

By applying this approximation, the potential Eq. (30) yields

$$\begin{aligned} \Delta \mathcal{I} = &\left[\int_{\mathcal{B}_0} \psi \, (\boldsymbol{F}, p) \ \mathrm{d}V \right]_{t=t_{n+1}} && - \left[\int_{\mathcal{B}_0} \psi \, (\boldsymbol{F}, p) \ \mathrm{d}V \right]_{t=t_n} \\ &+ \left[\int_{\mathcal{B}_0} f_{\text{dw}}(p, \nabla p) \, \overline{\psi} \left(\overline{\boldsymbol{F}}(\boldsymbol{F}, \boldsymbol{N}(\nabla p)) \right) \mathrm{d}V \right]_{t=t_{n+1}} && - \left[\int_{\mathcal{B}_0} f_{\text{dw}}(p, \nabla p) \, \overline{\psi} \left(\overline{\boldsymbol{F}}(\boldsymbol{F}, \boldsymbol{N}(\nabla p)) \right) \mathrm{d}V \right]_{t=t_n} \\ &+ \left[\int_{\mathcal{B}_0} h(p) \, \mathrm{d}V \right]_{t=t_{n+1}} && - \left[\int_{\mathcal{B}_0} h(p) \, \mathrm{d}V \right]_{t=t_n} \end{aligned} \tag{32}$$

$$
\begin{aligned}
&- \mathcal{W}_{\text{ext}}(t_{n+1}) && + \mathcal{W}_{\text{ext}}(t_n) \\
&+ \int_{\mathcal{B}_0} \Delta t\, \phi \left(\frac{p(t_{n+1}) - p(t_n)}{\Delta t} \right) \mathrm{d}V .
\end{aligned}
$$

For better readability in the time-discrete setting, the time index $n+1$ of the unknowns will be omitted, i.e., a missing index indicates the next time step t_{n+1}.

3.5. Stationarity and constitutive relations

Although the model has so far been mostly denoted in terms of $\boldsymbol{F}$, p and ∇p, the FE implementation will be set up to employ the motion $\boldsymbol{\varphi}$ and the phase field p as the only solution variables, on which $\boldsymbol{F}$ and ∇p directly depend. The unknown variables follow from stationarity of the potential as

$$
\{\boldsymbol{\varphi},\, p\} = \arg \inf_{\boldsymbol{\varphi},\, p} \{\Delta \mathcal{I}\} . \tag{33}
$$

The stationarity conditions itself then read in a variational form

$$
\delta_{\boldsymbol{\varphi}} \Delta \mathcal{I} = \int_{\mathcal{B}_0} \frac{\partial(\psi + \overline{\psi}_{\text{dw}})}{\partial \boldsymbol{F}} : \delta_{\boldsymbol{\varphi}} \boldsymbol{F}\, \mathrm{d}V - \int_{\mathcal{B}_0} \rho_0\, \boldsymbol{B} \cdot \delta \boldsymbol{\varphi}\, \mathrm{d}V - \int_{\mathcal{B}_0} \boldsymbol{T} \cdot \delta \boldsymbol{\varphi}\, \mathrm{d}A \overset{!}{=} 0 \tag{34}
$$

for the displacements/motion field $\boldsymbol{\varphi}$ and (using the Taylor-Voigt assumption)

$$
\delta_p \Delta \mathcal{I} = \int_{\mathcal{B}_0} \frac{\partial(\psi + \overline{\psi}_{\text{dw}} + h + \Delta t\, \phi)}{\partial p}\, \delta p\, \mathrm{d}V + \int_{\mathcal{B}_0} \frac{\partial \overline{\psi}_{\text{dw}}}{\partial \nabla p} \cdot \delta_p \nabla p\, \mathrm{d}V \overset{!}{=} 0 \tag{35}
$$

for the phase field parameter p, see e.g. [41]. Only non-vanishing terms were denoted here.

Assuming homogeneous Neumann boundary conditions (for p), the localization theorem applied to Eq. (35) yields the driving forces for the phase change. They write in the form of a variational derivative with respect to the phase field parameter p

$$
\delta_p \psi = \frac{\partial \psi}{\partial p} \delta p, \qquad \delta_p \overline{\psi} = \left[\frac{\partial \overline{\psi}}{\partial p} + \frac{\partial \overline{\psi}}{\partial \nabla p} \cdot \frac{\partial \nabla p}{\partial p} \right] \delta p. \tag{36}
$$

The first contribution is the driving force due to the bulk energies, e.g., because one bulk phase may be preferred due to energetically favorable elastic parameters. The second contribution drives phase changes due to the interface energy that depends on the phase field parameter and its gradient. The probably simplest example is that of interface-minimizing surface tension. A numerical example can be found in Section 5.1, where the contrast between dominating bulk and dominating interface contributions is discussed. The induced phase transformations are of displacive type and in contrast to, e.g., diffuse phase transformations.

For the diffuse phase field description, the system's dissipation inequality, $\mathcal{D} \geq 0$, is expressed in terms of dual conjugates and can be obtained for the isothermal case as a Clausius-Duhem (or rather Clausius-Planck) inequality [42]

$$
\begin{aligned}
\mathcal{D} = &\quad \mathcal{D}_0 && + \mathcal{D}_\phi \\
= &\quad \boldsymbol{P} : \dot{\boldsymbol{F}} - \pi\, \dot{p} + \boldsymbol{\xi} \cdot \nabla \dot{p} - [\dot{\psi} + \dot{\overline{\psi}}_{\text{dw}} + \dot{h}] && + \phi.
\end{aligned} \tag{37}
$$

$\mathcal{D}_0$ captures the conservative elastic and phase field contributions, while $\mathcal{D}_\phi$ is associated with the dissipation induced by phase transformations. The latter one once again shows that $\mathcal{I}$ is a pseudo-potential rather than a genuine one. $\boldsymbol{P}$ denotes the first Piola-Kirchhoff stress tensor, π represents a micro force and $\boldsymbol{\xi}$ the corresponding micro stresses (dual to ∇p).

In the next step, the Coleman-Noll procedure [28] is applied. By considering all internal dependencies in terms of $\boldsymbol{F}$, p and ∇p, this yields

$$
\mathcal{D} = \left[\boldsymbol{P} - \frac{\partial(\psi + \overline{\psi}_{\text{dw}})}{\partial \boldsymbol{F}} \right] : \dot{\boldsymbol{F}} + \left[-\pi - \frac{\partial(\psi + \overline{\psi}_{\text{dw}} + h)}{\partial p} \right] \dot{p} + \phi + \left[\boldsymbol{\xi} - \frac{\partial(\psi + \overline{\psi}_{\text{dw}})}{\partial \nabla p} \right] \cdot \nabla \dot{p}. \tag{38}
$$

The model's thermodynamically consistent constitutive relations then become, to comply with $\mathcal{D} \geq 0$, the following:

$$
\boldsymbol{P} = \frac{\partial(\psi + \overline{\psi}_{\text{dw}})}{\partial \boldsymbol{F}} = \frac{\partial \psi}{\partial \boldsymbol{F}} + \frac{\partial \overline{\psi}_{\text{dw}}}{\partial \overline{\boldsymbol{F}}} : \frac{\partial \overline{\boldsymbol{F}}}{\partial \boldsymbol{F}} = \frac{\partial \psi}{\partial \boldsymbol{F}} + \frac{\partial \overline{\psi}_{\text{dw}}}{\partial \overline{\boldsymbol{F}}} : \overline{\boldsymbol{I}} \tag{39}
$$

is the first Piola-Kirchhoff stress tensor. The first term corresponds to the classical bulk stresses. The second term represents the interface stresses, including an in-plane projection via $\overline{\boldsymbol{I}}$ (cf. Eq. (3)). For the micro stresses the procedure yields

$$
\boldsymbol{\xi} = \frac{\partial(\psi + \overline{\psi}_{\text{dw}})}{\partial \nabla p} \overset{\text{TV}}{=} \frac{\partial \overline{\psi}_{\text{dw}}}{\partial \nabla p}, \tag{40}
$$

where the Taylor-Voigt assumption (abbreviated as TV, cf. Section 3.2) renders the bulk-part in $\boldsymbol{\xi}$ to be independent of the phase field gradient ∇p.

The micro forces π are linked to the rate of the phase field variable and thus also to the dissipation functional ϕ. The choice of the latter must fulfill the (remaining) dissipation inequality $\mathcal{D}_\phi \geq 0$. Based on the work in [35], the dissipation functional is chosen of Ginzburg-Landau type, reading

$$
\phi = \frac{1}{2}\, \eta\, \dot{p}^2. \tag{41}
$$

The material parameter η represents the corresponding viscosity of the material against phase transformations. The functional renders the system rate dependent and the quadratic term guarantees that $\mathcal{D}_\phi \geq 0$ holds. The micro forces are then interpreted as a generalized dissipative force associated with the phase motion.

3.6. Prototype models

Hyperelastic bulk and interface materials are chosen as prototype models for the investigation of the previously introduced deformation-dependent interfaces, following the study of interface effects in [14]. Since the framework is designed for dealing with large deformations, energy contributions of neo-Hooke type are used. The Helmholtz energies of the bulk phases i are a function of the right Cauchy-Green tensor $\boldsymbol{C}_i = \boldsymbol{F}_i^{\mathrm{T}} \cdot \boldsymbol{F}_i$ and read

$$\psi_i = \frac{\mu_i}{2}\left[\mathrm{Tr}\left(\boldsymbol{C}_i\right) - n_{\mathrm{dim}}\right] - \mu_i \ln\left(\sqrt{\mathrm{Det}\left(\boldsymbol{C}_i\right)}\right) + \frac{\lambda_i}{2}\left[\ln\left(\sqrt{\mathrm{Det}\left(\boldsymbol{C}_i\right)}\right)\right]^2. \tag{42}$$

They are parameterized in terms of the Lamé parameters μ_i and $\lambda_i = \mu_i(E_i - 2\,\mu_i)/(3\,\mu_i - E_i)$, where μ_i is the shear modulus and E_i is Young's modulus. The later examples will particularly investigate various ratios of bulk elasticity in terms of λ_2/λ_1 and μ_2/μ_1, i.e., covering combinations of stiffer and softer bulks phases. The constant n_{dim} refers to the number of dimensions and is set to $n_{\mathrm{dim}} = 3$ for the later three-dimensional problems.

For the interface itself, a neo-Hooke like energy

$$\overline{\psi} = \overline{\psi}_0 + \frac{\bar{\mu}}{2}\left[\mathrm{Tr}\left(\overline{\boldsymbol{C}}\right) - [n_{\mathrm{dim}} - 1] - 2\,\ln\left(\sqrt{\overline{\mathrm{Det}}\left(\overline{\boldsymbol{C}}\right)}\right)\right] \tag{43}$$

was chosen. It consists of a constant part $\overline{\psi}_0$ and a part depending on the interface deformation in terms of invariants of $\overline{\boldsymbol{C}} = \overline{\boldsymbol{F}}^{\mathrm{T}} \cdot \overline{\boldsymbol{F}}$. To be more precise, it depends on invariants $\mathrm{Tr}(\overline{\boldsymbol{C}})$ and $\overline{\mathrm{Det}}(\overline{\boldsymbol{C}})$ and thus, the frame-indifferent energy is also isotropic. Particular focus will be given to the influence of $\overline{\psi}_0$ and, most importantly in this work, to the deformation-dependent contribution via $\bar{\mu}$.

4. Finite element implementation

The framework developed in the previous sections for diffuse interfaces was implemented into a finite element framework. This sections deals with the necessary steps, starting from the continuum model. The stationarity conditions constitute the starting point and can be reformulated in terms of a global residual

$$\boldsymbol{r} = \begin{bmatrix} \boldsymbol{r}_{\boldsymbol{\varphi}} \\ r_p \end{bmatrix} := \begin{bmatrix} \delta_{\boldsymbol{\varphi}} \Delta I \\ \delta_p \Delta I \end{bmatrix} \overset{!}{=} \begin{bmatrix} \boldsymbol{0} \\ 0 \end{bmatrix}. \tag{44}$$

To solve this fully coupled problem, the body $\mathcal{B}$ is first split into n_{el} subdomains or rather finite elements in a classic FE manner (for this and the following paragraphs refer to [43]), i.e.

$$\mathcal{B} \approx \bigcup_{e=1}^{n_{\mathrm{el}}} \mathcal{B}^e. \tag{45}$$

Each element is represented by n_{en} nodal points, at which the global fields for the motion $\boldsymbol{\varphi}$ and the order parameter for the phase field parameter p are discretized. For the approximation of any of the field values at an arbitrary point P with the coordinates $\boldsymbol{X}_{\mathrm{P}}$, the fields' $\{\bullet\}$ value $\{\bullet\}_{\mathrm{P}}$ is interpolated within the respective element e by using the nodal values $\{\bullet\}_A$. Shape functions N_A of (tri-)linear type are employed, such that $\{\bullet\}_{\mathrm{P}}$ reads

$$\{\bullet\}_{\mathrm{P}} \approx \sum_{A=1}^{n_{\mathrm{en}}} \{\bullet\}_A\, N_A(\boldsymbol{X}_{\mathrm{P}}) \tag{46}$$

and the corresponding gradient is approximated analogously to

$$\nabla_{\boldsymbol{X}} \{\bullet\}_{\mathrm{P}} = \frac{\partial \{\bullet\}_{\mathrm{P}}}{\partial \boldsymbol{X}} \approx \sum_{A=1}^{n_{\mathrm{en}}} \{\bullet\}_A \frac{\partial N_A(\boldsymbol{X}_{\mathrm{P}})}{\partial \boldsymbol{X}} = \sum_{A=1}^{n_{\mathrm{en}}} \{\bullet\}_A\, \nabla_{\boldsymbol{X}} N_A(\boldsymbol{X}_{\mathrm{P}}). \tag{47}$$

The specific interpolation schemes for the global fields and the gradient based quantities then read

$$\begin{aligned} \boldsymbol{X}^e &\approx \sum_{A=1}^{n_{\mathrm{en}}} N_A\, \boldsymbol{X}_A, \qquad \boldsymbol{\varphi}^e \approx \sum_{A=1}^{n_{\mathrm{en}}} N_A\, \boldsymbol{\varphi}_A, \qquad p^e \approx \sum_{A=1}^{n_{\mathrm{en}}} N_A\, p_A, \\ \boldsymbol{F}^e &\approx \sum_{A=1}^{n_{\mathrm{en}}} \boldsymbol{\varphi}_A \otimes \nabla N_A, \qquad \nabla p^e \approx \sum_{A=1}^{n_{\mathrm{en}}} p_A\, \nabla N_A. \end{aligned} \tag{48}$$

The same interpolation scheme is also applied to the variations $\delta\boldsymbol{\varphi}$, δp (also known as test functions) in Eqs. (34) and (35).

Another noteworthy approximation is that of the normal vector based on the phase field gradient of the last time step as

$$\boldsymbol{N}(t_{n+1}) \approx \boldsymbol{N}(t_n) = \left[\frac{\nabla p}{\|\nabla p\|}\right]_{t=t_n}. \tag{49}$$

It significantly reduces the computational effort by avoiding the implicit dependency on the yet unknown phase field, cf. [35].

With this at hand, the stationarity conditions Eqs. (34) and (35) can be rewritten for the FE algorithm to read

$$\delta_{\boldsymbol{\varphi}} \Delta I^e_{\text{red}} = \sum_{A=1}^{n_{\text{en}}} \delta \boldsymbol{\varphi}_A \cdot \left[\boldsymbol{f}^{eA}_{\text{int}\,\boldsymbol{\varphi}} - \boldsymbol{f}^{eA}_{\text{vol}\,\boldsymbol{\varphi}} - \boldsymbol{f}^{eA}_{\text{sur}\,\boldsymbol{\varphi}} \right], \qquad \delta_p \Delta I^e_{\text{red}} = \sum_{A=1}^{n_{\text{en}}} \delta p_A \, f^{eA}_{\text{int}\,p} \tag{50}$$

within the referential domain $\mathcal{B}^e_0$ of each element e [41]. The force contributions therein are defined as

$$\boldsymbol{f}^{eA}_{\text{int}\,\boldsymbol{\varphi}} = \int_{\mathcal{B}^e_0} \boldsymbol{P} \cdot \nabla N_A \, \mathrm{d}V, \qquad f^{eA}_{\text{int}\,p} = \int_{\mathcal{B}^e_0} -\pi \, N_A \, + \, \boldsymbol{\xi} \cdot \nabla N_A \, \mathrm{d}V \quad \left(\text{with} \;\; \pi = -\frac{\partial \Delta I}{\partial p}, \; \boldsymbol{\xi} = \frac{\partial \overline{\psi}_{\text{dw}}}{\partial \nabla p} \right) \tag{51}$$

for the internal forces, as well as

$$\boldsymbol{f}^{eA}_{\text{vol}\,\boldsymbol{\varphi}} = \int_{\mathcal{B}^e_0} N_A \, \boldsymbol{B} \, \mathrm{d}V, \qquad \boldsymbol{f}^{eA}_{\text{sur}\,\boldsymbol{\varphi}} = \int_{\mathcal{B}^e_0} N_A \, \boldsymbol{T} \, \mathrm{d}V \tag{52}$$

for the volumetric and surface force contributions.

Once the contributions for all elements are assembled into global vectors, the global residual reads

$$\mathbf{r} = \begin{bmatrix} \mathbf{r}_{\boldsymbol{\varphi}} \\ \mathbf{r}_p \end{bmatrix} := \begin{bmatrix} \mathbf{f}_{\text{int}\,\boldsymbol{\varphi}} - \mathbf{f}_{\text{vol}\,\boldsymbol{\varphi}} - \mathbf{f}_{\text{sur}\,\boldsymbol{\varphi}} \\ \mathbf{f}_{\text{int}\,p} \end{bmatrix} \overset{!}{=} \mathbf{0}. \tag{53}$$

In order to solve this coupled set of non-linear equations, a standard Newton-Raphson scheme is applied, i.e. the equation

$$\mathbf{K} \cdot [\Delta \underline{\boldsymbol{\varphi}} \;\; \Delta \underline{p}]^{\mathrm{T}} = -\mathbf{r} \tag{54}$$

is solved for the global vectors of unknowns denoted as $\Delta \underline{\boldsymbol{\varphi}}$ and $\Delta \underline{p}$. These are used to update the global list of nodal values for motion and order parameter with iteration counter k

$$\begin{bmatrix} \underline{\boldsymbol{\varphi}} \\ \underline{p} \end{bmatrix}_{k+1} = \begin{bmatrix} \underline{\boldsymbol{\varphi}} \\ \underline{p} \end{bmatrix}_{k} + \begin{bmatrix} \Delta \underline{\boldsymbol{\varphi}} \\ \Delta \underline{p} \end{bmatrix}, \tag{55}$$

iteratively, until the residual is sufficiently small.

Under the assumption of dead loads, the stiffness matrix $\mathbf{K}$ can be obtained from linearization of the internal forces. Analogous to the procedure above, the stiffness matrix of each element e then reads

$$\boldsymbol{K}^e = \sum_{A=1}^{n_{\text{en}}} \sum_{B=1}^{n_{\text{en}}} \begin{bmatrix} \boldsymbol{K}^{eAB}_{\boldsymbol{\varphi}\boldsymbol{\varphi}} & \boldsymbol{K}^{eAB}_{\boldsymbol{\varphi}p} \\ \boldsymbol{K}^{eAB}_{p\boldsymbol{\varphi}} & K^{eAB}_{pp} \end{bmatrix} \tag{56}$$

with

$$\begin{aligned} \boldsymbol{K}^{eAB}_{\boldsymbol{\varphi}\boldsymbol{\varphi}} &= \int_{\mathcal{B}^e_0} \nabla N^A \bullet \frac{\mathrm{d}\boldsymbol{P}}{\mathrm{d}\boldsymbol{F}} \cdot \nabla N^B \, \mathrm{d}V, \\ \boldsymbol{K}^{eAB}_{\boldsymbol{\varphi}p} &= \int_{\mathcal{B}^e_0} \frac{\mathrm{d}\boldsymbol{P}}{\mathrm{d}p} \cdot \nabla N^A \, N^B + \left[\frac{\mathrm{d}\boldsymbol{P}}{\mathrm{d}\nabla p} \cdot \nabla N^B \right] \cdot \nabla N^A \, \mathrm{d}V, \qquad \boldsymbol{K}^{eAB}_{p\boldsymbol{\varphi}} = \boldsymbol{K}^{eAB\,\mathrm{T}}_{\boldsymbol{\varphi}p}, \\ K^{eAB}_{pp} &= \int_{\mathcal{B}^e_0} \frac{\mathrm{d}(\partial_p \Delta I)}{\mathrm{d}p} \, N^A \, N^B + \frac{\mathrm{d}\boldsymbol{\xi}}{\mathrm{d}p} \cdot \left[\nabla N^A \, N^B + \nabla N^B \, N^A \right] + \nabla N^A \cdot \frac{\mathrm{d}\boldsymbol{\xi}}{\mathrm{d}\nabla p} \cdot \nabla N^B \, \mathrm{d}V \end{aligned} \tag{57}$$

for the element-wise contributions of node B with respect to node A. The global stiffness matrix $\mathbf{K}$ is obtained by assembling the element contributions $\boldsymbol{K}^e$.

Due to the underlying variational structure (minimization of an incremental energy), the resulting stiffness matrix is symmetric $\mathbf{K} = \mathbf{K}^{\mathrm{T}}$. The resulting non-linear set of equations has been solved by a monolithic Newton-scheme. It should be noted that staggered schemes – depending on the application, e.g. [44] – provide an alternative to reduce the risk of numerical instabilities, but were not required for the present elastic and viscous parameter sets. Tests comparing parametrization for an academic example were moreover performed for a spherical inclusion problem as shown in Appendix A.1.

With the coupled mechanical phase field model and its numerical implementation at hand, they will now be employed for numerical examples in the subsequent sections. Two specific boundary value problems will be considered to illustrate impact of deformation-dependent, elastic interfaces.

5. Coalescence of circular inclusions

This example analyzes the coalescence of two circular inclusions and serves two purposes. First, the main characteristics of the setup and the phase evolution due to the competition between bulk energy and constant interface energy are analyzed. Subsequently a deformation-dependent interface energy is introduced and its particular impact on the stress response in the transition zone is investigated. The model and the underlying algorithm are set up in full 3d. The examples mimic a 2d plane-stress setting, though, for a demonstrative investigation of the phase evolution without additional interference with the third spatial direction. Full 3d simulations have been employed, nevertheless, for benchmark and convergences studies (see Appendix).

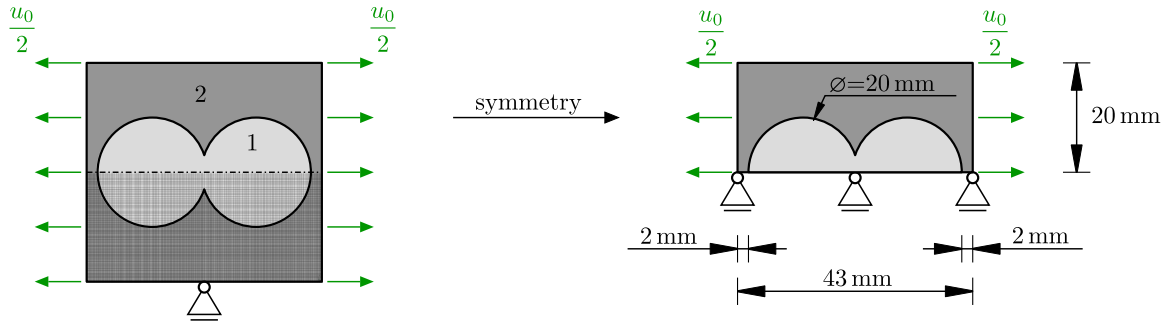

Fig. 3. The boundary value problem for the first numerical example: Two circular inclusions within a matrix material. The plate has a homogeneous thickness of $t = 1$ mm. The left side also shows the finite element mesh on the lower half. The right side shows the symmetry boundary conditions employed for the computations.

Table 1
The (material) parameters for the simulations of the numerical example of the coalescence of two inclusions. The bulk elastic moduli correlate to Young's moduli of $E_2 = 210$ GPa and $E_1 = 21$ GPa, respectively, as well as a Poisson's ratio of $\nu = 0.3$. The interface has a constant energy in the first example.

		Parameter	Symbol	Value	Unit
Bulk	Inclusion ($p = 0$)	1st Lamé parameter	λ_1	12 115	MPa
		2nd Lamé parameter	μ_1	8 077	MPa
	Matrix ($p = 1$)	1st Lamé parameter	λ_2	121 153	MPa
		2nd Lamé parameter	μ_2	80 769	MPa
Interface		Const. energy	$\overline{\psi}_0$	80/800/2000	MPa
		Elasticity parameter	$\overline{\mu}$	0	MPa
		Width	w	1.0	mm
Dissipation		Viscosity	η	40.0	MPa s
Penalty		Penalty parameter	h_{pen}	10^8	MPa
Loading		Prescribed displacements (linear over t until $t = 0.5$ s)	u_0	1.0	mm
		Load/time increments	Δt	10^{-3}	s

5.1. Coalescence of two circular inclusions with constant interface energy

5.1.1. Boundary value problem

Two circular inclusions within a matrix material constitute the first example, see Fig. 3. This boundary value problem is set up in a 3d environment and the boundary conditions ensure a plane-stress setting. The two inclusions overlap barely, but just enough, so that it will be possible to observe a coalescence of the two within the matrix material, without assigning any initial momentum or rather velocity for them to collide. In order to save computation time, the system's symmetry is exploited, which results in only the upper half of this domain being set up in the simulation. The left and right edges of the domain are loaded by prescribed displacements u_0 (applied linearly over time), which cause mainly tensile deformations and stresses in horizontal direction. On the lower bound, the vertical displacements are restricted to account for the symmetry and the upper edge (as well as all remaining nodes) are free, i.e. Neumann boundary conditions. In terms of the phase field, all nodes are subject to homogeneous Neumann boundary conditions (equivalent to $\nabla p \cdot \boldsymbol{N}_{\text{boundary}} = 0$), i.e. no prescribed values for p.

The boundary value problem still yields an FE mesh of approximately 35k tri-linear Hex8 elements. Symmetry is not assumed with respect the vertical plane to avoid a potential bias of the results, e.g., suppressing opposed shrinking and growing of inclusions. Nevertheless, such an asymmetric evolution was finally not observed.

The matrix material and the inclusion consist of two different elastic materials with a stiffness ratio of 10:1. The constant interface energy varies in this introductory example by $\overline{\psi}_0 = 80/800/2000$ MPa. It yet does not depend on strain to first focus the basic competing influences between bulk and interface on the phase evolution. See Table 1 for more details and refer to Section 3.6 for the prototype model equations of neo-Hooke type.

5.1.2. Results: Competing driving forces of bulk and interface

There are two main opposed driving forces present here, namely those based on the bulk and the interface, which both arise from energy minimization. The bulk mechanics dominate for the lowest interface energy, i.e., for the value of $\overline{\psi}_0 = 80$ MPa. While the initial evolution shows a slight coalescence, the overall phase transformation is governed by a spreading of the inclusion phase, see the top row in Fig. 4. The inclusion phase is more compliant and thus energetically favorable for the system. Phase transformation first occurs in vertical direction starting from both inclusions. It adapts to the horizontal loading and reduces the

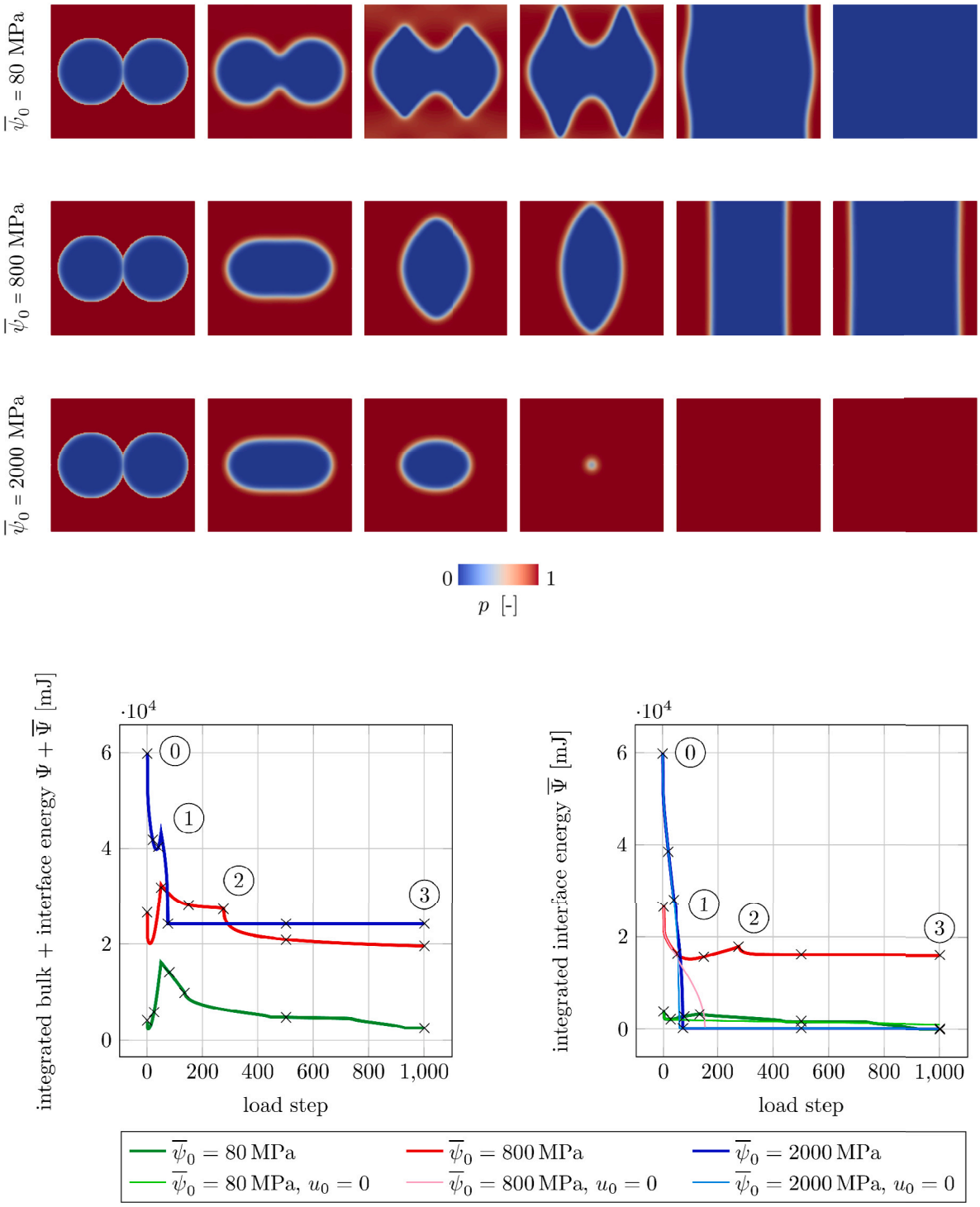

Fig. 4. Phase transformation of two soft inclusions for varying constant interface energy $\overline{\psi}_0$ (top) and the associated total and interface energies over time (bottom), where the ×-symbols indicate the incremental steps at which the evolution figures in the top were generated. The diagram on the lower right additionally features results for free boundaries with $u_0 = 0$.

associated stiffness of the overall structure. This not only depends on the volume fractions within the considered domain itself, but also on the distribution of deformations/stresses within this domain, because regions subjected to higher deformations are more costly in terms of bulk energy. Subsequently, the phase transformation continues also in the horizontal direction until the entire domain consists of only the softer inclusion phase. The evolution in the third direction is homogeneous due to the (plane stress) boundary conditions and hence not explicitly depicted. The explicit energy evolution (bottom graphs in Fig. 4) accordingly shows an increase of total energy due to the increase in loading (between ⓪ and ①), followed by a continuous relaxation due to the bulk phase transformations (between ① and ③). The interface energy then remains comparably small and constant.

Increasing the interface energy towards $\overline{\psi}_0 = 800\,\text{MPa}$ amplifies the coalescence effect, see the middle row of the evolution figures in Fig. 4. Both inclusions coalesce first, before the inclusion phase starts to spread from the united inclusion domain. From this point, the bulk transformation continues as before, first in vertical direction and then in horizontal direction. Much more remarkably, the energy course shows a distinct interface influence. At the very first load steps, the total energy and the interface energy drop due to the reduction of interface area by coalescence. This effect superposes the influence of loading and is much faster. Later (②), a distinctive kink in the energies again denotes the contact of the interface with the boundaries. This is a coalescence effect across the symmetric boundaries. The specific times of these coalescence events are governed by the elastic moduli, the viscosity of the Ginzburg-Landau dissipation potential and the distance of the interfaces.

The highest interface energy of $\overline{\psi}_0 = 2000\,\text{MPa}$ finally allows the interface to dominate. The initial coalescence reduces the energy much more than is induced by the loading (between ⓪ and ①). The inclusion also shrinks quickly to a circular shape, see the third row of the evolution figures in Fig. 4. In contrast to the previous two settings, the bulk phase transformation into the inner, more compliant and therefore preferred phase, is suppressed. Instead, the driving force of interface minimization is so strong that the inner compliant phase vanishes completely. The sensitivity with respect to bulk and interface energies also matches the observations in literature, for instance the evolution in martensitic microstructures [45] or the arms spacing in dendritic growth [46], showing the feasibility of the framework to capture the competition between the individual effects.

In order to separate interface and bulk contributions more clearly, the three simulations have also been conducted without any prescribed loads, i.e. $u_0 = 0$. This leads to the absence of any deformations and the problem is purely driven by the constant interface energy term (thinner lines in the lower right plot of Fig. 4). The difference to the loaded case is mostly notable during the middle and the final stages of the phase evolution, where the bulk had its highest impact. Without any induced deformation, the softer inclusion phase does not spread out anymore and the interface shrinks over time until it finally vanishes in all cases. The transformation rate plausibly correlates with the interface parameter.

5.2. Coalescence of two circular inclusions with deformation-dependent interface energy

5.2.1. Boundary value problem

While the previous part studied the basic effects by assuming a deformation-independent interface energy ($\overline{\mu} = 0$), this part compares it to the case of deformation dependence ($\overline{\mu} = 100\,\text{GPa}$). The geometry and load conditions remain identical, see again Fig. 3. As the previous case of $\overline{\psi}_0 = 800\,\text{MPa}$ allowed to observe the characteristic influence of both the bulk and the interface, this value of constant interface energy will be used for the remainder of this example section. The bulk elasticity ratio will be varied though (by factors 10^{-1}, 10^{0} and 10^{+1}), because the interface stress response showed a notable sensitivity in this regard. See Table 2 for the numerical values.

Table 2
The (material) parameters for the simulations of the numerical example of the coalescence of two inclusions for the deformation-dependent interface model. Parameters, which are not respecified here, remain as stated in Table 1.

		Parameter	Symbol	Value	Unit
Bulk	General	1st Lamé parameter	$\tilde{\lambda}$	121 153	MPa
		2nd Lamé parameter	$\tilde{\mu}$	80 769	MPa
	Inclusion	1st Lamé parameter	λ_1	$\tilde{\lambda}/\tilde{\lambda}/\frac{\tilde{\lambda}}{10}$	
	($p = 0$)	2nd Lamé parameter	μ_1	$\tilde{\mu}/\tilde{\mu}/\frac{\tilde{\mu}}{10}$	
	Matrix	1st Lamé parameter	λ_2	$\frac{\tilde{\lambda}}{10}/\tilde{\lambda}/\tilde{\lambda}$	
	($p = 1$)	2nd Lamé parameter	μ_2	$\frac{\tilde{\mu}}{10}/\tilde{\mu}/\tilde{\mu}$	
Interface		Const. energy	$\overline{\psi}_0$	800	MPa
		Elasticity parameter	$\overline{\mu}$	0/100	GPa

5.2.2. Results: Stress localization induced by deformation-dependent interface energy

For the sake of comparability, the deformation-dependent interface contribution was chosen to be moderate such that the evolution of the phases remained qualitatively similar, see the evolution series of all parameter variations in Fig. 5. Along this phase evolution, a time step at the beginning of the coalescence event is used for detailed comparison (single magnified contour plots in Fig. 5). Larger values of deformation-dependent interface energy generally strengthen the effects of interface elasticity as observed in the previous analysis of competing bulk and interface contributions.

The general impact of the interface is observed on different time intervals. While it only takes very little time until the interface energy rounds off corners in the present example (Fig. 4), its influence on the systems stiffness is more persistent. The latter becomes observable in the stress fields around the phase transition zone that change on a larger time scale. Indeed, in comparison to the

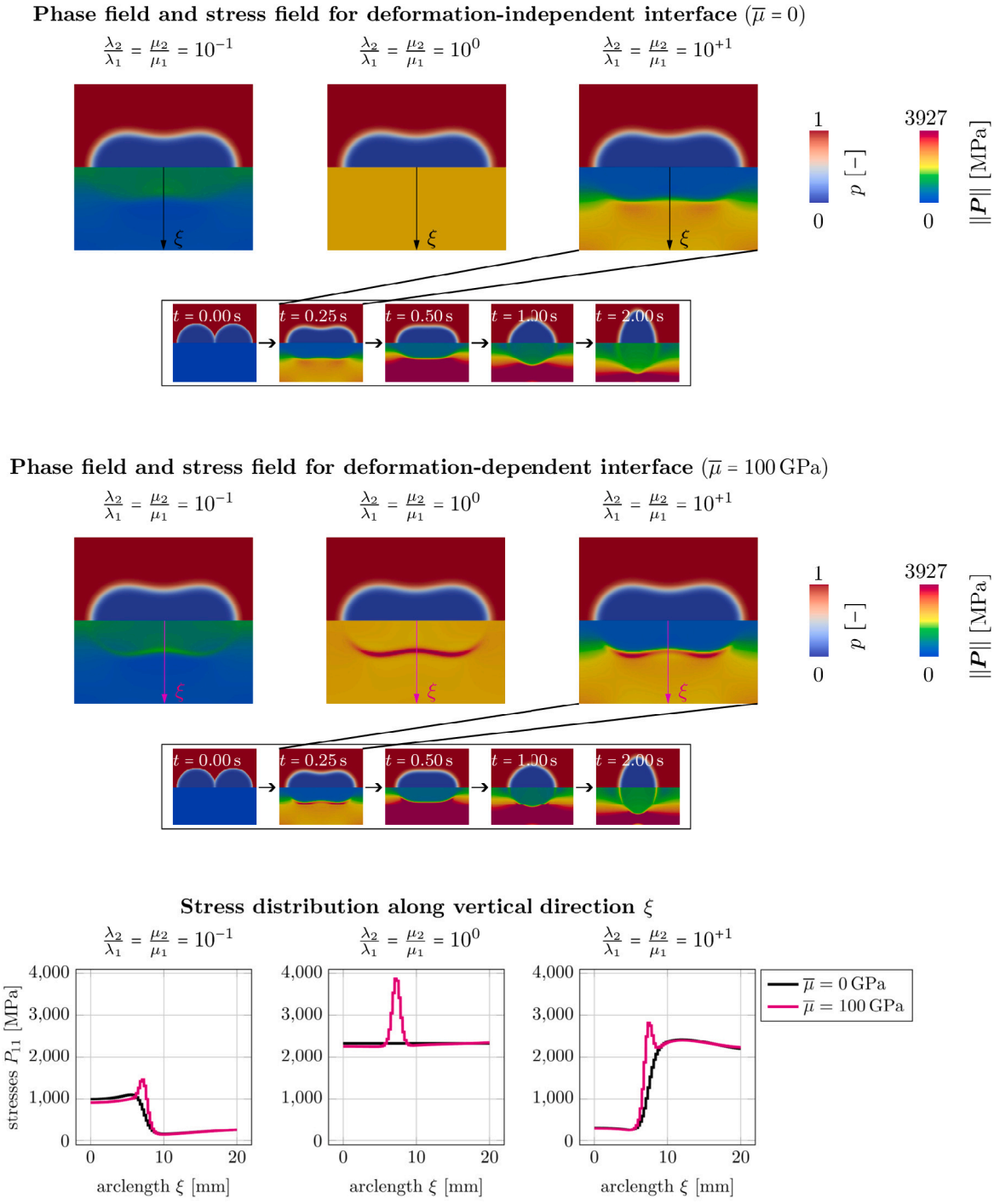

Fig. 5. Top: Phase field p and the norm of the first Piola-Kirchhoff stresses $\boldsymbol{P}$ for combinations of strain-dependent interface energy and bulk elasticity ratio (in both the bulk phases and the interface). Bottom: P_{11} along arc length for deformation-dependent energy vs. deformation-independent energy ($\overline{\mu} = 100\,\mathrm{GPa}$ vs. $\overline{\mu} = 0\,\mathrm{GPa}$) at time $t = 0.25\,\mathrm{s}$.

surrounding bulk phases, the interface induces zones of magnified stresses (in terms of the norm of the first Piola-Kirchhoff stresses $\boldsymbol{P}$). They are particularly pronounced for the horizontally oriented part of the interface. Only the particular case of identical bulk phases and strain-independent interface energies shows a completely homogeneous stress field. The horizontal alignment of all other intensified stress fields around the transition zone is due to the tangential (in-plane) interface elasticity. The interface thus adapts to

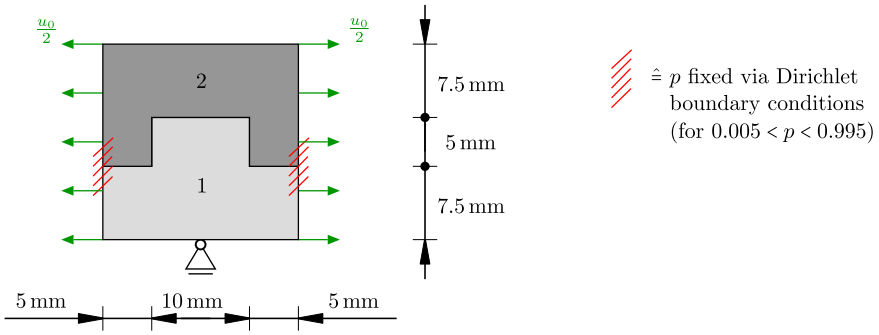

Fig. 6. The boundary value problem for the second numerical example: A quadratic block with a protrusion of the compliant phase into the stiffer phase, yielding a stepped interface. The plate has a homogeneous thickness of $t = 0.1$ mm.

the load direction and creates an overall anisotropic response. The deformation-dependence enhances this effect by more than 50% or even activates it for identical bulk properties. The deformation dependence can thus become relevant for anisotropic natural or designed effective properties [47] of materials and structures [48].

The detailed course of the horizontal stresses (P_{11}) shows that the deformation-dependence induces an additional stress peak, that is in the order of bulk stresses (magenta lines in Fig. 5 compared to black lines for deformation-independent interfaces). Observations at grain boundaries of crystalline structures [49] or at the surface of pores [50] also indicate the appearance of such stress deviations beyond the present synthetic parameter variations. Deformation-dependent elasticity of free copper surfaces was also derived on the basis of atomistic simulations [4,5,51] and accompanied by relaxation processes of the atoms' positions and energy fields near the interface. Such localized stresses can become particularly relevant for effects inside or near the phase boundary, e.g., interface-mediated diffusion or chemistry-related interactions that are susceptible to stress-induced structural changes on smaller scales [52]. The effect of local stress increase is moreover observed for all stiffness ratios of the bulk phases.

6. Breakup of a stepped interface

6.1. Boundary value problem

This example complements the previous one by a stronger focus on the interface itself and a breakup event instead of coalescence. The body is once again a 3d-plate with a homogeneous thickness, where boundary conditions enforce a plane-stress setting, see Fig. 6. It is discretized by exactly 30k finite elements of type Hex8. A stepped interface separates the stiffer phase at the bottom from the compliant phase at the top. Sharp corners are used here to better capture the curvature-minimizing tendency that is known from classical capillary effects. The stiffness ratio of bulk elastic moduli is 10:1, which previously showed the highest overall sensitivity to interface and bulk contributions. The interface elasticity varies in terms of the deformation-dependent parameter $\overline{\mu}$ between 0 and 500 GPa. The specific parameters can be found in Table 3, in case they deviate from the previous setup in Table 1. The loading is again applied on the left and right edges in the form of prescribed displacements u_0. It increases linearly in time and remains fixed after 0.5 s.

The interface is pinned on the left and right side to complement the previous example of freely evolving phases across the boundaries. To be more precise, the phase field is fixed by Dirichlet boundary conditions on the left and right edge around the phase transition region (where $0.005 < p < 0.995$). It ensures that the interface remains subjected to the deformation caused by the external loads. If not pinned, the interface would favor a downward translation to diminish the lower less compliant phase, which is more similar to the shrinking process of the former example. The stepped geometry additionally allows to investigate the simultaneous effect of smoothing corners, which is already well-known from classic interface minimization. Besides of that, the phase field parameter is again free to evolve, i.e. p is subject to Neumann boundary conditions ($\nabla p \cdot \boldsymbol{N}_{\text{boundary}} = 0$) other than the marked areas.

6.2. Results: Rounding corners, stretching and delayed breakup

The first evolution of the initial state ⓪ is a rounding of the corners and a corresponding reduction of interface area, see Fig. 7. As the strains did not significantly evolve yet, this process is governed by the constant interface energy that is equal in all settings. Afterward, the increasing external load raises the energy until its maximum ①. A larger deformation-dependent interface energy accordingly also causes a larger total energy along this stretching process, during which the interface flattens. The accompanying phase transformation is supported by the bulk's tendency to favor the compliant upper phase. The characteristic times show little sensitivity to the interface energy during these steps of the example. The employed dissipation moreover limits higher transformation rates, even though they can be energetically favored for large driving forces in terms of $\overline{\mu}$.

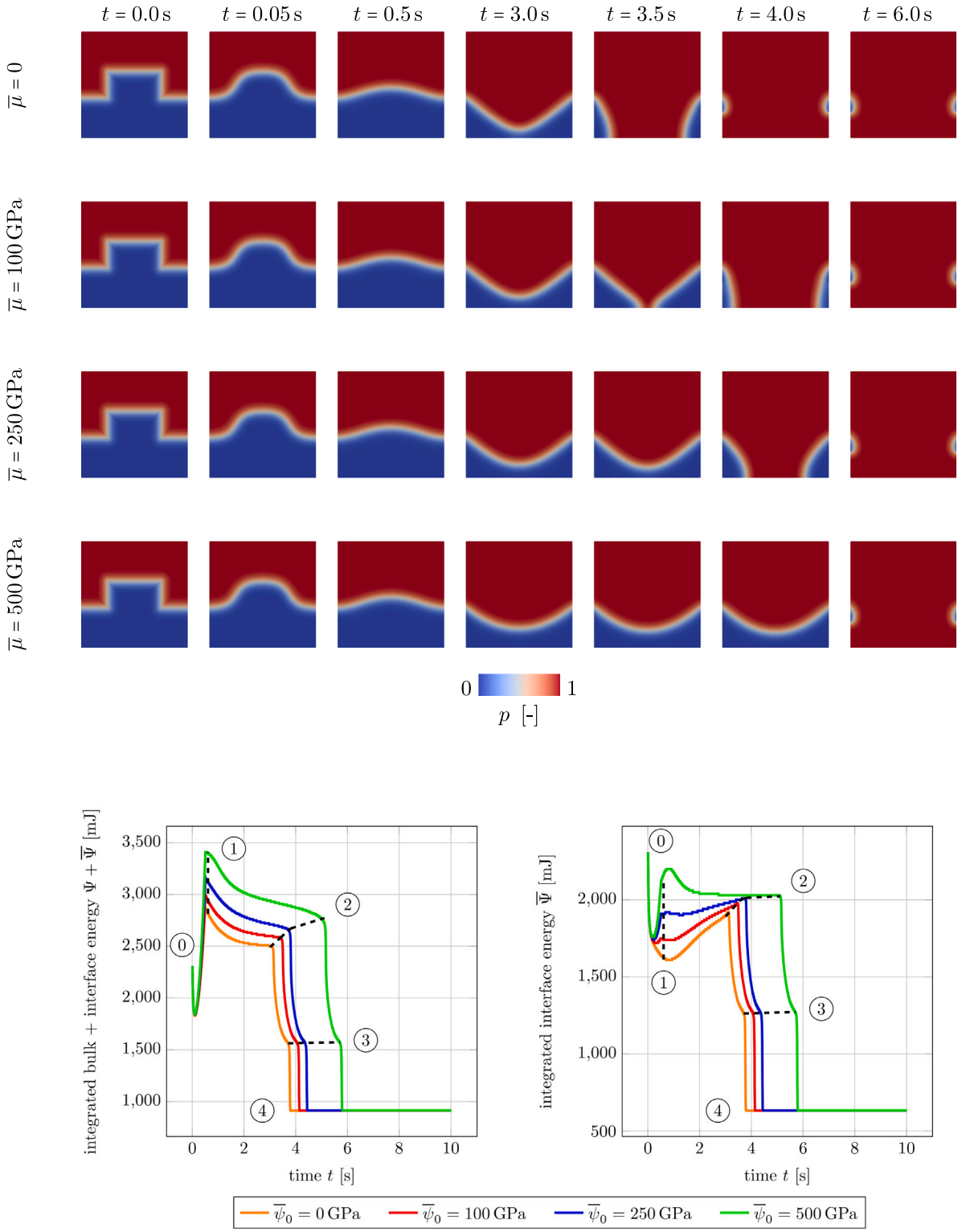

Fig. 7. Breakup of a stepped interface between an upper compliant and a lower stiff bulk phase for varying deformation-dependent interface energies via $\overline{\mu}$ (top) and the associated total and interface energies over time (bottom).

Table 3
The (material) parameters for the simulations of the numerical example of the stepped interface. Parameters, which are not respecified here, remain as stated in Table 1.

		Parameter	Symbol	Value	Unit
Bulk	Stiff	1st Lamé parameter	λ_1	121 153	MPa
	($p = 0$)	2nd Lamé parameter	μ_1	80 769	MPa
	Compliant	1st Lamé parameter	λ_2	12 115	MPa
	($p = 1$)	2nd Lamé parameter	μ_2	8 077	MPa
Interface		Const. energy	$\overline{\psi}_0$	800	MPa
		Elasticity parameter	$\overline{\mu}$	0/100/250/500	GPa
Loading		Prescribed displacements (linear over t until $t = 0.5$ s)	u_0	0.5	mm

The subsequent breakup process stands out by its sensitivity with respect to the deformation-dependent interface elasticity; in terms both of duration and energy (between ① and ②). It should first be noted that bulk and interface yield partially opposite driving forces for the phase evolution. The bulk phases always try to increase the portion of the upper compliant phase. As the phase transition is pinned on the left and right side, their separation line bends towards the bottom. The course of the total energy gradually decreases during this phase transformation, cf. Fig. 7. The constant part of the interface energy, on the contrary, tries to maintain a flat shape with minimum area. The course of the participating interface energies hence mostly increases for low deformation dependency (cf. $\overline{\mu} = 0$ GPa), after a short transition time. This increase can be explained by the mere increase of interface area, because no additional loading is added after ①. That effect is however reversed, in turn, for large deformation dependency (cf. $\overline{\mu} = 500$ GPa), which shows a decrease in interface energy after a short transition. Moreover, the duration until final breakup is considerably longer. It originates from the deformation-dependence of the interface that adds to the overall stiffness of the system. The interface resists the horizontal stretch more for deformation-dependent energies. This is similar to the deformation-dependent elasticity of the bulk phases that finally show a breakup. In view of the opposing driving forces due to bulk and interface elasticity, parameter modifications would also allow to stabilize the system before break-up and terminate the evolution at an earlier stage in Fig. 7; also see other systems where interfaces dictate stability and geometry such as Rayleigh-Taylor instabilities [53] or the size distribution of spherical vesicles [54].

After breakup, all systems again behave similarly during the disappearance of the stiffer phase (between ② and ④) that is mainly accompanied by a relatively fast interface reduction. A kink can be observed in the energy courses (at ③), where the phase boundary leaves the bottom edge. After that point, the stiffer bulk phase and the interface area are reduced only by a vertical motion along the sides, perpendicular to the load direction.

Among the observed effects, the deformation-dependent interface elasticity stands out by its influence on the breakup event. Its duration or characteristic energy peaks may help to assess the values of $\overline{\mu}$ and its relevance for practical applications. The determination of material constants for interfaces can be challenging due to superposing bulk phenomena and a possible restriction to smaller scales [5]. The presented framework and academic results can hence also aim at supporting the identification of suitable geometries, loading conditions and times for sensitivity and calibration studies.

7. Conclusion

In the work at hand, a variationally consistent framework was introduced for the combined consideration of interface elasticity and mechanically induced phase transformations. The framework was obtained by use of an Allen-Cahn type phase field model into a three-dimensional large-strain continuum formulation. The coherent and diffuse interface description was based on a Modica-Mortola double well functional. The phase field approximation of the interface deformation gradient has been derived by means of homogenization theory. It was shown, that three homogenization approaches at the interface do not cause a jump of the interface deformation gradient between the phases, because of the in-plane projection: Taylor-Voigt, rank-1 and partial rank-1. Subsequently the Taylor-Voigt homogenization scheme was chosen for the work at hand. The model furthermore included a viscosity or rather dissipation formulation of Ginzburg-Landau type linked to phase transformation. It was then discretized in time and space in a variationally consistent manner and implemented into a FE framework. The resulting set of non-linear coupled equations was solved by means of a monolithic Newton-scheme. Compared to other investigations, special emphasis was put on the role of the deformation-dependent interface elasticity.

A coalescence and a breakup scenario were investigated in numerical experiments. The former one was utilized to show the underlying, competing driving forces resulting in accelerated coalescence for higher interface energies. It was also shown that interface energy can counteract otherwise favorable bulk-induced phase transformations. Deformation-dependent interface energies caused significant, in-plane stress peaks when compared to their pure bulk counterparts. They are therefore able to noticeably influence the systems stiffness in terms of amplitude and direction.

In the latter breakup example it was moreover shown, that the interface elasticity influences the systems compliance and consequentially the time scale in such processes. While the initial behavior was practically not altered, the eventual rupture event was shifted significantly in time, depending on the interface elasticity that depends on the interface strain itself. This makes it a promising approach for parameter identification purposes in real experiments.

The practical relevance of interface elasticity must moreover be evaluated in future studies of real systems, for which calibration poses an extra challenge due to possibly limited sensitivities. The present framework and parameter variations aim at supporting this task by highlighting the sensitivity of characteristic events. In case the elastic limits would be exceeded, the observed stress augmentation of deformation-dependent interface elasticity can even become critical, for example, when triggering damage mechanisms [55–57]. On the other hand, highly elastic interfaces such as coatings or protective interlayers may help to bear extensive stresses, e.g. [58]. Future work will aim at the incorporation of inelastic interface behavior to broaden the class of interface materials.

CRediT authorship contribution statement

Hendrik Wilbuer: Writing – review & editing, Writing – original draft, Visualization, Software, Methodology, Investigation, Conceptualization. **Patrick Kurzeja:** Writing – review & editing, Supervision, Methodology. **Jörn Mosler:** Writing – review & editing, Supervision, Methodology, Conceptualization.

Declaration of competing interest

The authors declare that they have no known competing financial interests or personal relationships that could have appeared to influence the work reported in this paper.

Data availability

Data will be made available on request.

Declaration of Generative AI and AI-assisted technologies in the writing process

Statement: During the preparation of this work the authors used DeepL in order to improve language, as well as ChatGPT 3.5 in order to generate shell scripts for automated batch trimming, rotation and positioning of graphics. After using this tool/service, the authors reviewed and edited the content as needed and take full responsibility for the content of the publication.

Acknowledgments

The authors gratefully acknowledge financial support from the German Research Foundation (DFG) via project “Phasenfeldbeschreibung allgemeiner imperfekter Grenzflächen” (401344875) as well as the computing time provided on the Linux HPC cluster at Technical University Dortmund (LiDO3), partially funded by the German Research Foundation (DFG) via the Large-Scale Equipment Initiative (271512359).

Appendix. Demonstration of basic model properties using a spherical inclusion problem

This appendix is concerned with the demonstration of basic properties of the model/framework. For this, a spherical inclusion problem is considered as a test case, see Fig. A.8. The inclusion and the outer shell are represented by two distinct phases separated by a diffuse interface. The inclusion, i.e. the inner sphere, is set to significantly lower elastic properties (by factor 100) as summarized in Table A.4. The outer surface of the sphere is loaded by uniformly distributed displacements u_0 in outward radial direction. The displacements are applied linearly over time until the maximum value is reached at $t = 0.5\,\mathrm{s}$. After that, the prescribed displacement is held and allows for inner relaxation in both the phase field p and the motion field $\boldsymbol{\varphi}$. The phase field is moreover prescribed to $p = 0$ in the center and to $p = 1$ on the outermost boundary.

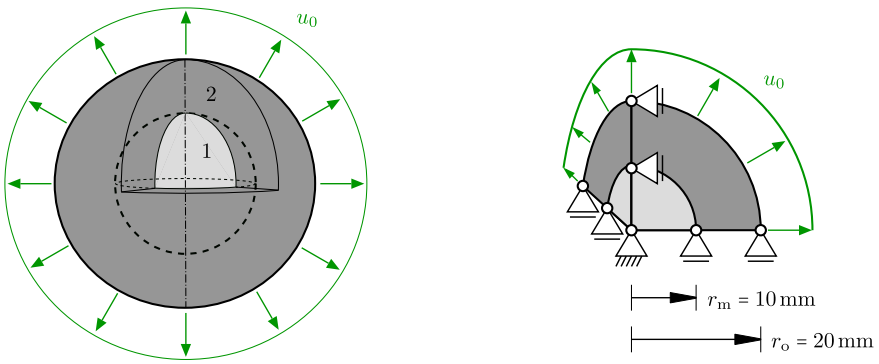

Fig. A.8. The boundary value problem for the third numerical example: a spherical inclusion problem. The outer sphere has a radius of $r_\mathrm{o} = 20\,\mathrm{mm}$ and is uniformly loaded with prescribed displacements u_0.

Table A.4
The (material) parameters for the simulations of the spherical inclusion problem. Parameters, which are not respecified here, remain as stated in Table 1.

		Parameter	Symbol	Value	Unit
Bulk	Phase 1	1st Lamé parameter	λ_1	1 212	MPa
	($p = 0$)	2nd Lamé parameter	μ_1	808	MPa
	Phase 2	1st Lamé parameter	λ_2	121 153	MPa
	($p = 1$)	2nd Lamé parameter	μ_2	80 769	MPa
Interface		Const. energy	$\overline{\psi}_0$	800	MPa
		Elasticity parameter	$\overline{\mu}$	200	GPa
Loading		Prescribed displacements (linear over t until $t = 0.5$ s)	u_0	0.5	mm

A.1. Comparison of parametrizations

In a first step, a comparison for a set of different parametrizations for the spherical inclusion problem will be considered. Specifically, four setups will be compared to test the framework, see Fig. A.9. They utilize the spherical symmetry both in geometry and loading. The first setup employs the default Cartesian parametrization as used for the above examples for a symmetric 1/8 of the body. The second setup employs spherical coordinates (r, θ, φ), which can be beneficial for the approximation of significant curvature and were tested for the same part. The third setup further harnesses the symmetry by a reduced 3d-spike. The fourth setup uses an efficient 1d description, because the complexity can practically be reduced to the spatial evolution in radial direction. It does not resemble the practical main framework, but acts as a reference with lowest computational effort and highest accuracy due to a finer discretization. (The 1d-model features 5k 1d-elements along the radius, whereas the full 1/8-sphere 3d-models consist of 207k Tet4 elements. The latter approximately equals 45 elements alongside the radius and hence represents a mesh with more than 100 times the average element edge length in comparison to the 1d-setup, while consuming vastly more computation time.)

The radial displacements u_r, the radial component of the deformation gradient F_{rr} as well as the first Piola-Kirchhoff stress components P_{rr}, $P_{\theta\theta} = P_{\varphi\varphi}$ were chosen exemplary for comparison at four different time steps in Fig. A.10. After the initialization, the interface first aims at reducing its area (see $t = 0.20$ s). Once the load increased sufficiently, the bulk energy driving force becomes dominant and leads to a phase transformation into the inner phase (see $t = 0.50$ s), i.e. the interface moves back outward. From that point on the bulk part stays dominant and the interface proceeds to the very outer shell (see $t = 1.00$ s). The interface does not vanish completely here, because the phase field was prescribed on the outer shell using boundary conditions.

The courses of the curves in each of the diagrams virtually overlap in most cases. The spherical 3d-variants show outliers at $r = 0$, most likely due to the singularity of the radial coordinate. The other, even smaller deviations are assumed to result from unequal interpolation for visualization of different parametrizations and discretization errors. For a much finer discretization as with the 1d-spike variant, they disappear.

In addition to the good match between the setups, the aforementioned physical effects of the main examples can also be observed (cf. Section 5.2.2). While the stresses in radial direction P_{rr}, i.e. in interface normal direction, do not show a significant super-elevation, the ones in tangential direction (i.e. $P_{\theta\theta}$ and $P_{\varphi\varphi}$) clearly do. In order to get a more detailed insight, Fig. A.11 contrasts the radial and tangential stresses for different values of the interface elasticity parameter $\overline{\mu}$. Although the curves in the diagram do all represent the same point in time $t = 0.4$ s, the interface position (as indicated by the jump in the stresses) is not the same for all variants, due to the effects discussed in Section 6.2. It can however be observed, that the super-elevation above the default tangential stresses is significant, if $\overline{\mu}$ is high enough.

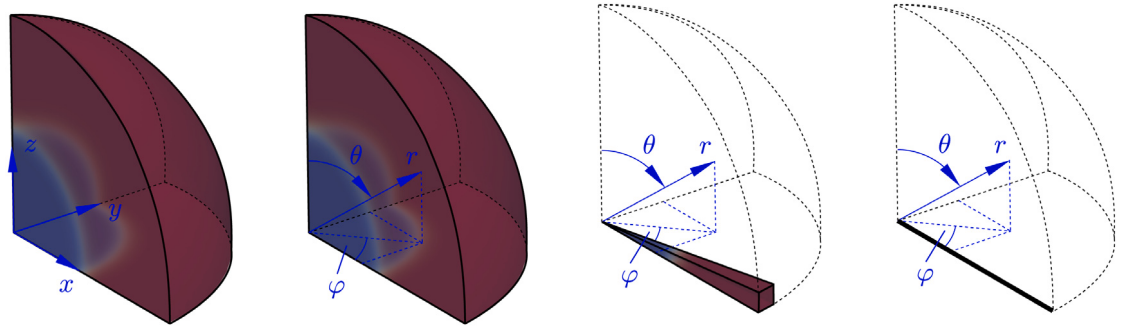

(a) 1/8-sphere with Cartesian coordinate system.

(b) 1/8-sphere with spherical coordinate system.

(c) 3d-spike with spherical coordinate system.

(d) 1d-spike or rather domain within 3d spherical coordinate system.

Fig. A.9. Illustration of the different simulation domains and their corresponding coordinate systems.

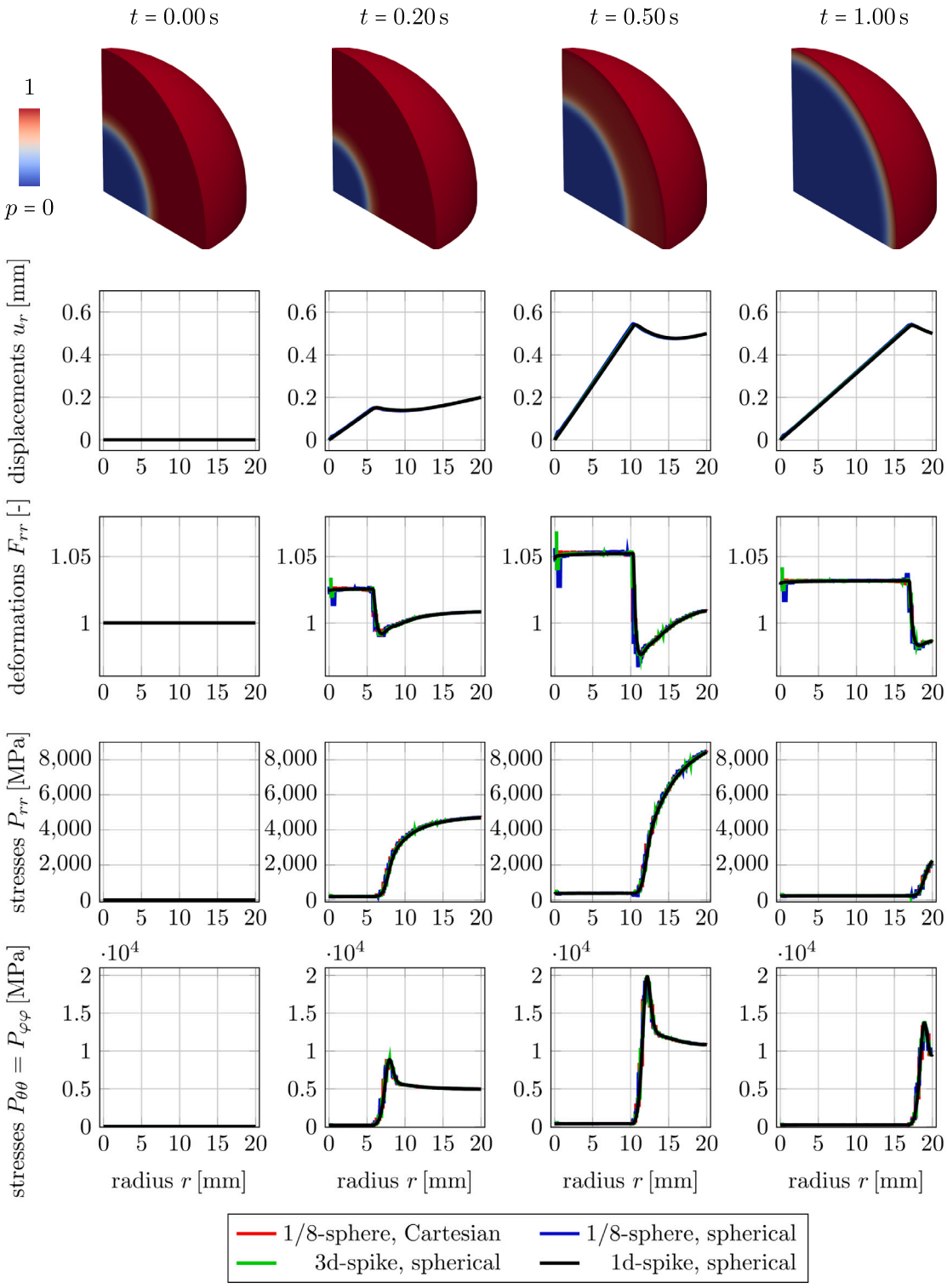

Fig. A.10. Comparison of the results for radial displacements u_r as well as the radial components of the deformation gradient F_{rr} and all normal stress components of the first Piola-Kirchhoff stresses P_{rr}, $P_{\theta\theta}$ and $P_{\varphi\varphi}$ for the different implementation variants (3d vs. 1d, spherical vs. Cartesian). Note that the results virtually overlap in most cases. The visualizations of the systems phase field states in the top row are exemplary and were taken from the Cartesian 3d-variant.

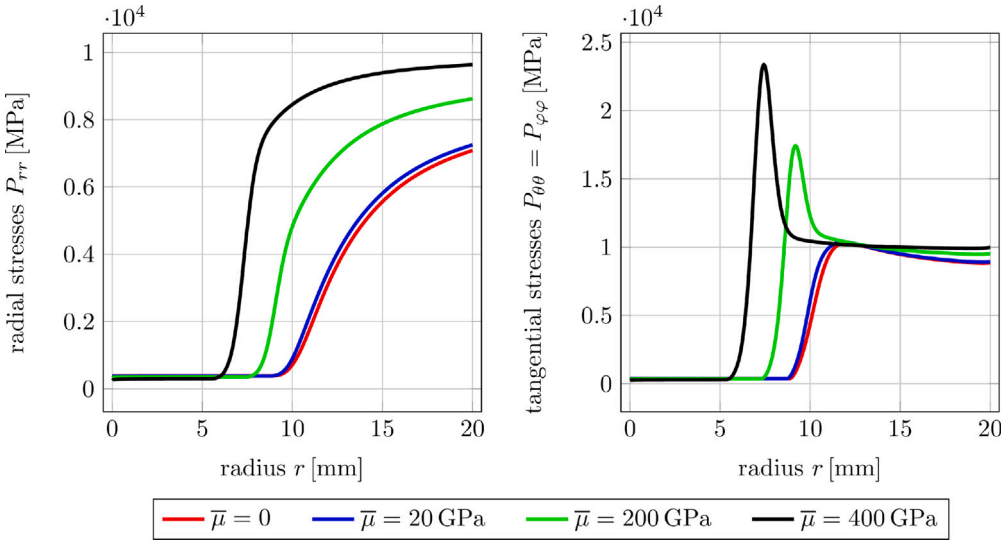

Fig. A.11. Illustration of the radial stresses P_{rr} and the tangential stresses $P_{\theta\theta} = P_{\varphi\varphi}$ over the radius r for various values of the interface elasticity parameter $\overline{\mu}$. The results were obtained from the 1d-variant of the algorithm. They represent the system's state at time $t = 0.4$ s.

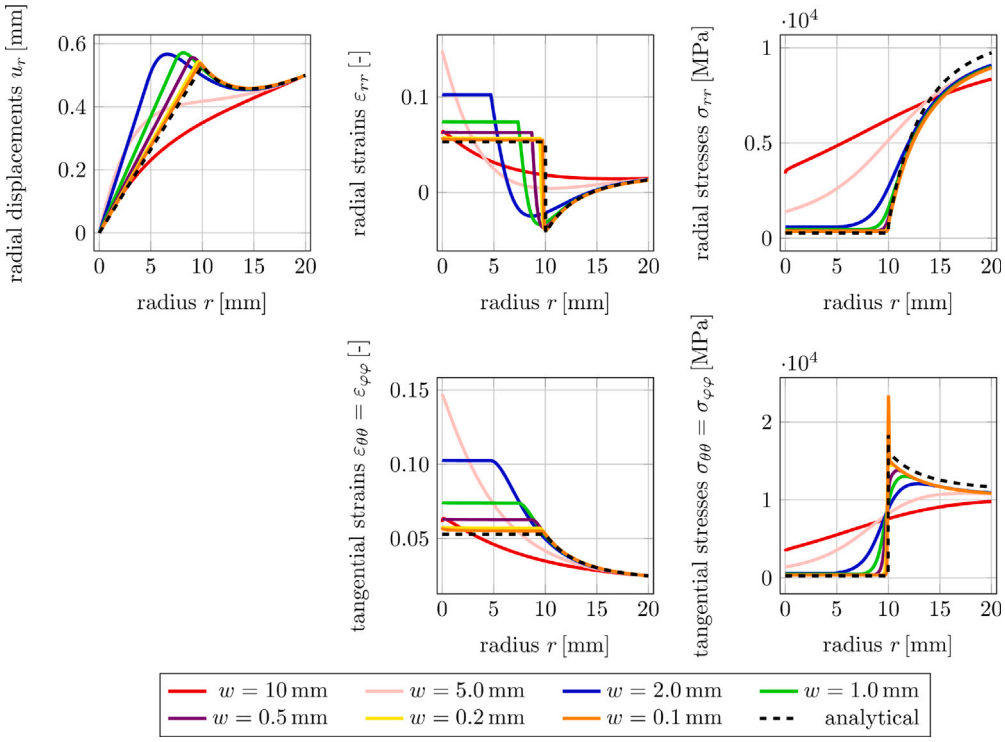

Fig. A.12. Illustration of the radial displacements u_r as well as the radial and tangential components of strains (ε_{rr}, $\varepsilon_{\theta\theta} = \varepsilon_{\varphi\varphi}$) and stresses ($\sigma_{rr}$, $\sigma_{\theta\theta} = \sigma_{\varphi\varphi}$) for a varied diffuse phase field width w in comparison to the analytical solution, using $\overline{\mu} = 20$ GPa. Due to the spherical symmetry, the tangential components of both stresses and strains are each identical. For the same reason $u_\theta = u_\varphi = 0$ holds everywhere, so that the corresponding diagram was omitted.

A.2. Convergence study

As denoted in Section 3.3, the diffuse interface approximates the sharp interface solution in the sense of convergence. This section features a brief numerical convergence study regarding the interface width w. It analyzes the boundary value problem of Appendix A.1 for a fixed order parameter, i.e. the rate $\dot{p} = 0$ now holds everywhere. This is enforced by further boundary conditions within the FE framework. Different interface widths w are compared to each other and additionally directly compared to an analytical sharp interface solution. The latter one has been determined based on Hooke's model in a small strain setting.

The results for a decreasing series of w can be found in Fig. A.12 and are expressed in terms of linearized strains and Cauchy stresses for a straightforward comparison with the analytical solution (maximum absolute strains are below 0.15 and only reach a few percent for the converging solutions, indicating a minor relevance of material and geometrical non-linearities of the prototype example). The convergence can be observed as anticipated. With decreasing values of w, the numerical phase field solutions close in on the analytical one. For displacements u_r and strains ϵ the lines for the smallest w and the analytical solution virtually overlap. Minor deviations only remain for stresses in the domain $r > 10\,\text{mm}$ that we attribute to the numerical inaccuracy and a remaining mismatch in terms of the assumption of linearity, while convergence is clearly observed.

References

[1] H.-J. Bargel (Ed.), Werkstoffkunde: Strukturen - grundlegende Eigenschaften, 13th ed., in: Springer-Lehrbuch, Springer Vieweg, Berlin, 2022.

[2] J. Gril, D. Jullien, S. Bardet, H. Yamamoto, Tree growth stress and related problems, J. Wood Sci. 63 (5) (2017) 411–432, http://dx.doi.org/10.1007/s10086-017-1639-y.

[3] F. Lolli, H. Manzano, J.L. Provis, M.C. Bignozzi, E. Masoero, Atomistic simulations of geopolymer models: The impact of disorder on structure and mechanics, ACS Appl. Mater. Interfaces 10 (26) (2018) 22809–22820, http://dx.doi.org/10.1021/acsami.8b03873.

[4] V.B. Shenoy, Atomistic calculations of elastic properties of metallic fcc crystal surfaces, Phys. Rev. B 71 (9) (2005) 094104, http://dx.doi.org/10.1103/PhysRevB.71.094104.

[5] C. Sievers, J. Mosler, L. Brendel, P. Kurzeja, Computational homogenization of material surfaces: From atomistic simulations to continuum models, Comput. Mater. Sci. 175 (2020) 109431, http://dx.doi.org/10.1016/j.commatsci.2019.109431.

[6] J. Han, D.J. Srolovitz, M. Salvalaglio, Disconnection-mediated migration of interfaces in microstructures: I. continuum model, Acta Mater. 227 (2022) 117178, http://dx.doi.org/10.1016/j.actamat.2021.117178.

[7] M. Salvalaglio, D.J. Srolovitz, J. Han, Disconnection-Mediated migration of interfaces in microstructures: II. diffuse interface simulations, Acta Mater. 227 (2022) 117463, http://dx.doi.org/10.1016/j.actamat.2021.117463.

[8] B. Jérme, A. Bosseboeuf, P. Pieranski, Anchoring of nematic liquid crystals on terraced silicon surfaces, Phys. Rev. A 42 (10) (1990) 6032–6041, http://dx.doi.org/10.1103/PhysRevA.42.6032.

[9] B. Buffel, F. Desplentere, K. Bracke, I. Verpoest, Modelling open cell-foams based on the Weaire–Phelan unit cell with a minimal surface energy approach, Int. J. Solids Struct. 51 (19–20) (2014) 3461–3470, http://dx.doi.org/10.1016/j.ijsolstr.2014.06.017.

[10] M.T. McDowell, S.W. Lee, J.T. Harris, B.A. Korgel, C. Wang, W.D. Nix, Y. Cui, In situ TEM of two-phase lithiation of amorphous silicon nanospheres, Nano Lett. 13 (2) (2013) 758–764, http://dx.doi.org/10.1021/nl3044508.

[11] M.E. Gurtin, A. Ian Murdoch, A continuum theory of elastic material surfaces, Arch. Ration. Mech. Anal. 57 (4) (1975) 291–323, http://dx.doi.org/10.1007/BF00261375.

[12] D.J. Steigmann, R.W. Ogden, Plane deformations of elastic solids with intrinsic boundary elasticity, Proc. R. Soc. Lond. Ser. A Math. Phys. Eng. Sci. 453 (1959) (1997) 853–877, http://dx.doi.org/10.1098/rspa.1997.0047.

[13] P. Steinmann, On boundary potential energies in deformational and configurational mechanics, J. Mech. Phys. Solids 56 (3) (2008) 772–800, http://dx.doi.org/10.1016/j.jmps.2007.07.001.

[14] A. Javili, P. Steinmann, J. Mosler, Micro-to-macro transition accounting for general imperfect interfaces, Comput. Methods Appl. Mech. Engrg. 317 (2017) 274–317, http://dx.doi.org/10.1016/j.cma.2016.12.025.

[15] G. Barenblatt, The formation of equilibrium cracks during brittle fracture. General ideas and hypotheses. Axially-symmetric cracks, J. Appl. Math. Mech. 23 (3) (1959) 622–636, http://dx.doi.org/10.1016/0021-8928(59)90157-1.

[16] D. Dugdale, Yielding of steel sheets containing slits, J. Mech. Phys. Solids 8 (2) (1960) 100–104, http://dx.doi.org/10.1016/0022-5096(60)90013-2.

[17] D.-H. Yeon, P.-R. Cha, J.-H. Kim, M. Grant, J.-K. Yoon, A phase field model for phase transformation in an elastically stressed binary alloy, Modelling Simul. Mater. Sci. Eng. 13 (3) (2005) 299–319, http://dx.doi.org/10.1088/0965-0393/13/3/001.

[18] G. Boussinot, Y. Le Bouar, A. Finel, Phase-field simulations with inhomogeneous elasticity: Comparison with an atomic-scale method and application to superalloys, Acta Mater. 58 (12) (2010) 4170–4181, http://dx.doi.org/10.1016/j.actamat.2010.04.008.

[19] S.M. Allen, J.W. Cahn, A microscopic theory for antiphase boundary motion and its application to antiphase domain coarsening, Acta Metall. 27 (6) (1979) 1085–1095, http://dx.doi.org/10.1016/0001-6160(79)90196-2.

[20] J.W. Cahn, J.E. Hilliard, Free energy of a nonuniform system. I. Interfacial free energy, J. Chem. Phys. 28 (2) (1958) 258–267, http://dx.doi.org/10.1063/1.1744102.

[21] N. Moës, J. Dolbow, T. Belytschko, A finite element method for crack growth without remeshing, Internat. J. Numer. Methods Engrg. 46 (1) (1999) 131–150, http://dx.doi.org/10.1002/(SICI)1097-0207(19990910)46:1<131::AID-NME726>3.0.CO;2-J.

[22] J.K. Knowles, Stress-induced phase transitions in elastic solids, Comput. Mech. 22 (6) (1999) 429–436, http://dx.doi.org/10.1007/s004660050376.

[23] O. Bouaziz, S. Allain, C. Scott, Effect of grain and twin boundaries on the hardening mechanisms of twinning-induced plasticity steels, Scr. Mater. 58 (6) (2008) 484–487, http://dx.doi.org/10.1016/j.scriptamat.2007.10.050.

[24] M.E. Gurtin, A. Ian Murdoch, Surface stress in solids, Int. J. Solids Struct. 14 (6) (1978) 431–440, http://dx.doi.org/10.1016/0020-7683(78)90008-2.

[25] A. Javili, N.S. Ottosen, M. Ristinmaa, J. Mosler, Aspects of interface elasticity theory, Math. Mech. Solids 23 (7) (2018) 1004–1024, http://dx.doi.org/10.1177/1081286517699041.

[26] C. Sievers, J. Mosler, P. Kurzeja, Projection vs. relaxation of adjacent bulk deformation for surface modeling: Theoretical and numerical aspects, Int. J. Solids Struct. 226–227 (2021) 111084, http://dx.doi.org/10.1016/j.ijsolstr.2021.111084.

[27] A. Javili, Thermomechanics of Solids accounting for Surfaces and Interfaces, in: Schriftenreihe Technische Mechanik, Lehrstuhl für Technische Mechanik, Universität Erlangen-Nürnberg, Erlangen, 2012, number 7/2012.

[28] B.D. Coleman, W. Noll, The thermodynamics of elastic materials with heat conduction and viscosity, Arch. Ration. Mech. Anal. 13 (1) (1963) 167–178, http://dx.doi.org/10.1007/BF01262690.

[29] P. Nozières, D.E. Wolf, Interfacial properties of elastically strained materials: I. Thermodynamics of a planar interface, Z. Phys. B 70 (3) (1988) 399–407, http://dx.doi.org/10.1007/BF01317248.

[30] D. Pino-Muñoz, J. Bruchon, S. Drapier, F. Valdivieso, Sintering at particle scale: An eulerian computing framework to deal with strong topological and material discontinuities, Arch. Comput. Methods Eng. 21 (2) (2014) 141–187, http://dx.doi.org/10.1007/s11831-014-9101-4.

[31] R. Peerlings, M. Geers, R. De Borst, W. Brekelmans, A critical comparison of nonlocal and gradient-enhanced softening continua, Int. J. Solids Struct. 38 (44–45) (2001) 7723–7746, http://dx.doi.org/10.1016/S0020-7683(01)00087-7.

[32] J.C. Simo, J. Oliver, F. Armero, An analysis of strong discontinuities induced by strain-softening in rate-independent inelastic solids, Comput. Mech. 12 (5) (1993) 277–296, http://dx.doi.org/10.1007/BF00372173.

[33] K. Langenfeld, P. Kurzeja, J. Mosler, How regularization concepts interfere with (quasi-)brittle damage: a comparison based on a unified variational framework, Contin. Mech. Thermodyn. 34 (6) (2022) 1517–1544, http://dx.doi.org/10.1007/s00161-022-01143-2.

[34] M. Ortiz, E. Repetto, Nonconvex energy minimization and dislocation structures in ductile single crystals, J. Mech. Phys. Solids 47 (2) (1999) 397–462, http://dx.doi.org/10.1016/S0022-5096(97)00096-3.
[35] A. Bartels, J. Mosler, Efficient variational constitutive updates for Allen–Cahn-type phase field theory coupled to continuum mechanics, Comput. Methods Appl. Mech. Engrg. 317 (2017) 55–83, http://dx.doi.org/10.1016/j.cma.2016.11.024.
[36] V. De Rancourt, K. Ammar, B. Appolaire, S. Forest, Homogenization of viscoplastic constitutive laws within a phase field approach, J. Mech. Phys. Solids 88 (2016) 291–319, http://dx.doi.org/10.1016/j.jmps.2015.12.026.
[37] J. Mosler, O. Shchyglo, H. Montazer Hojjat, A novel homogenization method for phase field approaches based on partial rank-one relaxation, J. Mech. Phys. Solids 68 (2014) 251–266, http://dx.doi.org/10.1016/j.jmps.2014.04.002.
[38] L. Modica, S. Mortola, Un esempio di Gamma-convergenza, in: Bollettino della Unione Matematica Italiana B, Vol. 14, 1977, pp. 285–299.
[39] L. Modica, The gradient theory of phase transitions and the minimal interface criterion, Arch. Ration. Mech. Anal. 98 (2) (1987) 123–142, http://dx.doi.org/10.1007/BF00251230.
[40] G. Dal Maso, An Introduction to Gamma-Convergence, Birkhäuser, Boston, MA, 1993, OCLC: 840277786.
[41] A. Bartels, P. Kurzeja, J. Mosler, Cahn–Hilliard phase field theory coupled to mechanics: Fundamentals, numerical implementation and application to topology optimization, Comput. Methods Appl. Mech. Engrg. 383 (2021) 113918, http://dx.doi.org/10.1016/j.cma.2021.113918.
[42] A. Bartels, Modelling of evolving microstructures at different scales, in: Schriftenreihe des Instituts für Mechanik, Institut für Mechanik, Technische Universität Dortmund, Dortmund, 2017, number 2017/02.
[43] P. Wriggers, Nonlinear Finite Element Methods, Springer, Berlin, 2008.
[44] C. Miehe, M. Hofacker, F. Welschinger, A phase field model for rate-independent crack propagation: Robust algorithmic implementation based on operator splits, Comput. Methods Appl. Mech. Engrg. 199 (45–48) (2010) 2765–2778, http://dx.doi.org/10.1016/j.cma.2010.04.011.
[45] V.I. Levitas, D.-W. Lee, D.L. Preston, Interface propagation and microstructure evolution in phase field models of stress-induced martensitic phase transformations, Int. J. Plast. 26 (3) (2010) 395–422, http://dx.doi.org/10.1016/j.ijplas.2009.08.003.
[46] T. Suzuki, M. Ode, S.G. Kim, W.T. Kim, Phase-field model of dendritic growth, J. Cryst. Growth 237–239 (2002) 125–131, http://dx.doi.org/10.1016/S0022-0248(01)01891-7.
[47] S. Saeb, P. Steinmann, A. Javili, On effective behavior of microstructures embedding general interfaces with damage, Comput. Mech. 64 (6) (2019) 1473–1494, http://dx.doi.org/10.1007/s00466-019-01727-x.
[48] U. Larsen, O. Signund, S. Bouwsta, Design and fabrication of compliant micromechanisms and structures with negative Poisson's ratio, J. Microelectromech. Syst. 6 (2) (1997) 99–106, http://dx.doi.org/10.1109/84.585787.
[49] Q. Zhao, Q. Zhu, Z. Zhang, X. Li, Q. Huang, W. Yang, J. Wang, H. Gao, H. Zhou, Imaging of atomic stress at grain boundaries based on machine learning, J. Mech. Phys. Solids 181 (2023) 105455, http://dx.doi.org/10.1016/j.jmps.2023.105455.
[50] M.A. Grekov, A.B. Vakaeva, W.H. Müller, Stress field around cylindrical nanopore by various models of surface elasticity, Contin. Mech. Thermodyn. 35 (1) (2023) 231–243, http://dx.doi.org/10.1007/s00161-022-01168-7.
[51] R. Dingreville, J. Qu, A semi-analytical method to compute surface elastic properties, Acta Mater. 55 (1) (2007) 141–147, http://dx.doi.org/10.1016/j.actamat.2006.08.007.
[52] E. Masoero, G. Di Luzio, Nanoparticle simulations of logarithmic creep and microprestress relaxation in concrete and other disordered solids, Cem. Concr. Res. 137 (2020) 106181, http://dx.doi.org/10.1016/j.cemconres.2020.106181.
[53] P.-G. De Gennes, F. Brochard-Wyart, D. Quéré, Capillarity and Wetting Phenomena, Springer, New York, NY, 2004, http://dx.doi.org/10.1007/978-0-387-21656-0.
[54] W. Helfrich, Size distributions of vesicles : the role of the effective rigidity of membranes, J. Physique 47 (2) (1986) 321–329, http://dx.doi.org/10.1051/jphys:01986004702032100.
[55] M.A. Wollenweber, C.F. Kusche, T. Al-Samman, S. Korte-Kerzel, On the automated characterisation of inclusion-induced damage in 16MnCrS5 case-hardening steel, Adv. Ind. Manuf. Eng. 7 (2023) 100123, http://dx.doi.org/10.1016/j.aime.2023.100123.
[56] O. Kintzel, J. Mosler, An incremental minimization principle suitable for the analysis of low cycle fatigue in metals: A coupled ductile–brittle damage model, Comput. Methods Appl. Mech. Engrg. 200 (45–46) (2011) 3127–3138, http://dx.doi.org/10.1016/j.cma.2011.07.006.
[57] P. Maruschak, R. Vorobel, O. Student, I. Ivasenko, H. Krechkovska, O. Berehulyak, T. Mandziy, L. Svirska, O. Prentkovskis, Estimation of fatigue crack growth rate in heat-resistant steel by processing of digital images of fracture surfaces, Metals 11 (11) (2021) 1776, http://dx.doi.org/10.3390/met11111776.
[58] H. Liu, L. Liang, Y. Wang, Y. Wei, Fracture characteristics and damage evolution of coating systems under four-point bending, Int. J. Appl. Ceram. Technol. 13 (6) (2016) 1043–1052, http://dx.doi.org/10.1111/ijac.12605.